

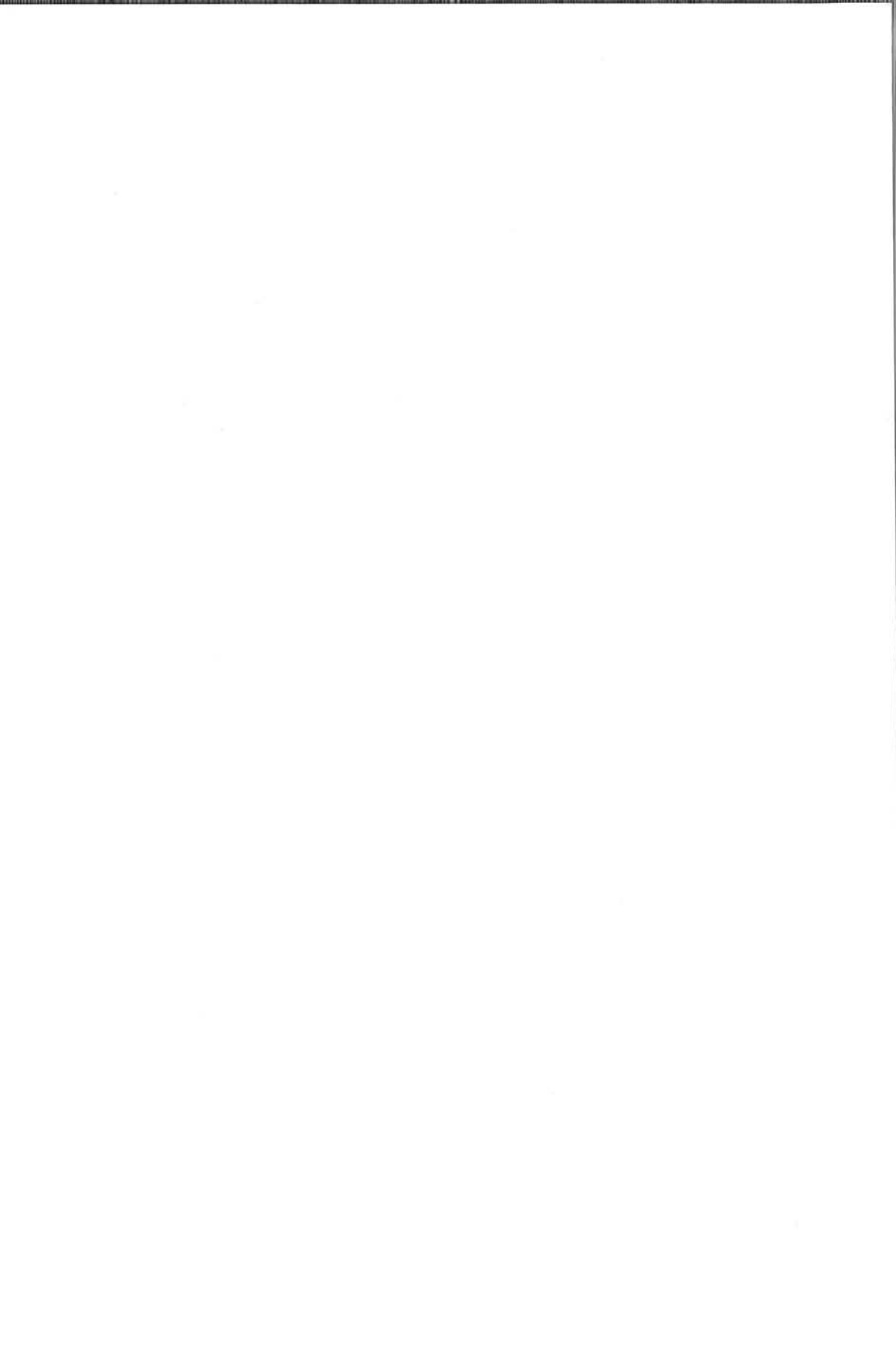
Series 01 Aerodynamics 07

Linear Temporal Stability Analysis

P.J.J. Moeleker



Delft University Press



706331

Linear Temporal Stability Analysis

Bibliotheek TU Delft



C 3021863

2392
347
5



Linear Temporal Stability Analysis

P.J.J. Moeleker



Delft University Press / 1998

Published and distributed by:

Delft University Press
Mekelweg 4
2628 CD Delft
The Netherlands
Telephone +31 (0)15 278 32 54
Fax +31 (0)15 278 16 61
e-mail: DUP@DUP.TUdelft.NL

by order of:

Faculty of Aerospace Engineering
Delft University of Technology
Kluyverweg 1
P.O. Box 5058
2600 GB Delft
The Netherlands
Telephone +31 (0)15 278 14 55
Fax +31 (0)15 278 18 22
e-mail: Secretariaat@LR.TUdelft.NL
website: <http://www.lr.tudelft.nl/>

Cover: Aerospace Design Studio, 66.5 x 45.5 cm, by:
Fer Hakkaart, Dullenbakkersteeg 3, 2312 HP Leiden, The Netherlands
Tel. +31 (0)71 512 67 25

90-407-1570-X

Copyright © 1998 by Faculty of Aerospace Engineering

All rights reserved.

No part of the material protected by this copyright notice may be reproduced or utilized in any form or by any means, electronic or mechanical, including photocopying, recording or by any information storage and retrieval system, without written permission from the publisher: Delft University Press.

Printed in The Netherlands

Contents

1	Introduction	1
2	Linear stability model	5
2.1	Navier-Stokes equations for power-law fluids	5
2.2	Orr-Sommerfeld for power-law fluids	7
2.3	Power-law fluid sheared by Blasius flow	9
2.4	No-slip at the wall	11
2.5	Location of the interface	11
2.6	Continuity of velocity	12
2.7	Dynamic boundary conditions	13
2.8	Conditions at infinity	15
2.9	Energy	16
2.10	Vorticity/enstrophy	18
2.11	Primary solution	19
3	Numerical analysis	25
3.1	Chebyshev polynomials	25

3.2	Numerical implementation	27
4	One-layer flow	33
4.1	One-layer Blasius flow	33
4.1.1	Numerical parameters	33
4.1.2	Stability curves	36
4.1.3	Perturbation quantities	39
4.1.4	Energy considerations	44
4.2	Calculations without the virtual interface	48
5	Two-layer flow	51
5.1	Air stream over anti-icing fluid	51
5.1.1	Stability curves	51
5.1.2	Perturbation quantities	54
5.1.3	Energy consideration	58
5.1.4	Parameters survey	60
5.2	Validation energy considerations	63
5.3	Comparison with literature	64
6	Conclusions	65
	References	67

Chapter 1

Introduction

Two-layer flows are very familiar phenomena in every-day life. Examples include an air stream over a sea surface or rain running down a window. A lot of effort has been put in research of these flows, especially in the situation that one of the flows is a thin liquid layer, due to the interest of industry. Two-layer flows show up in, for example, distillation columns, condensers, pipe flows and photographic emulsions. The dynamics of the thin fluid layer has a considerable effect on transport rates of mass, heat and momentum.

The flow over an airfoil covered with a thin layer of liquid, more specific a de- or anti-icing fluid, is the main interest of this research. Several experiments on wings covered with a de- or anti-icing fluids have shown a considerable lift loss and drag increase, see for example [1] and [8]. It was argued that these adverse effects were a result of the formation of waves on the liquid surface, which as a consequence leads to a thickening of the boundary layer. Based on these observations, the Von Kármán Institute (Brussels, Belgium) developed an aerodynamic acceptance test for de- and anti-icing fluids in the eighties. Just recently, they have also increased their efforts on the theoretical side of the problem [29] [32].

At Delft University of Technology, an effort has started to predict the dynamical behaviour of an air stream over a de- or anti-icing fluid deposited on an airfoil. As indicated by experimental results, waves will form on the surface of the thin liquid layer when air starts to flow over it. The formation and growth of waves can be split in an initial phase, where the first very small waves will appear on the air-liquid interface and a growth phase, where the amplitudes

of the waves become finite. The linear stability analysis that follows, characteristic for the initial phase, has to determine under which conditions waves will start to grow and which waves will appear. This linear stability analysis has already received considerable attention in the literature.

At the end of the last century, Stokes, Kelvin and Rayleigh managed to adapt the stability analysis of a dynamical system of (point) masses to a continuum (flow) by adding small perturbations to a steady-state solution. The resulting stability equation for the Navier-Stokes equations is nowadays referred to as the Orr-Sommerfeld equation after Orr [27] and Sommerfeld [36] who independently obtained an analytic solution for the stability of plane Couette flow at the beginning of this century. Squire [37] showed that for a two-dimensional steady-state solution two-dimensional disturbances are more unstable than three-dimensional disturbances, i.e., by considering the fully two-dimensional problem the most conservative estimate will be obtained.

Amongst the pioneers of the treatment of the eigenvalue problem based on the Orr-Sommerfeld equation was Feldman [10]. Feldman considered the stability of two viscous incompressible fluids of which one was bounded by a solid wall and the other one was unbounded, assuming a linear basic velocity profile in each layer. The linear basic velocity made the Orr-Sommerfeld equation suitable for (partial) analytical analysis. Yih [40] considered a two-layer flow bounded by two solid walls which can move relatively to each other. He obtained analytical solutions for long waves. Kao [18] performed a similar analysis for the case that a free surface bounded the top fluid layer.

However, most of the literature on linear stability concentrates on film waves, neglecting the dynamic behaviour of the fluid above. Lin [21] gives an excellent review article on these film waves. Just recently, several articles appeared on the linear stability of two-layer flows. Miesen and Boersma [23] considered a thin liquid layer flowing down a vertical plane sheared by a gas layer. They used a parabolic velocity distribution in the liquid film and approximated the velocity distribution in the gas layer by a linear part and a part with constant velocity. To obtain neutral stability curves, they approximate the unknown functions by Chebyshev polynomials. This method, first used by Orszag [28], will also be used here to compute the solution of the Orr-Sommerfeld equation numerically.

Yih [41] investigated analytically the formation of waves on a liquid of high viscosity (de-icing fluid) sheared by an air stream. The discrepancy between

his results and the numerical results in chapter 5 of the present report are mainly caused by the assumptions Yih made to obtain analytical closed form expressions for both the speed and the growth rate of the waves. Amongst others, he assumed that the ratio of the dynamic viscosity of the liquid to that of the gas is very high, while in the present numerical analysis this assumption is not made.

At the Von Kármán Institute, Rumberg [32] considered an infinite flat plate covered with a thin layer of liquid sheared by an air stream and used a shooting method to compute the stability curves. He also considered the stability of an isolated air stream (Blasius boundary-layer profile) in order to validate his results and to establish the effect of the thin liquid layer. His results are in agreement with the ones presented in chapters 4 and 5 of this report. Özgen [29] extended the results of Rumberg to liquids of the class of non-Newtonian power-law fluids (as a model for an anti-icing fluid). As will be shown in the next chapter, his interface condition requiring continuity of normal stress appears to be incorrect.

Chapter 2

Linear stability model

2.1 Navier-Stokes equations for power-law fluids

For the two-dimensional flow of an incompressible fluid, the Navier-Stokes equations consist (here) of the continuity equation and momentum equations in x - and y -direction and can be written as [33],

$$\frac{\partial u^*}{\partial x^*} + \frac{\partial v^*}{\partial y^*} = 0, \quad (2.1)$$

$$\frac{\partial u^*}{\partial t^*} + u^* \frac{\partial u^*}{\partial x^*} + v^* \frac{\partial u^*}{\partial y^*} = -\frac{1}{\rho^*} \frac{\partial p^*}{\partial x^*} + \frac{1}{\rho^*} \frac{\partial \tau_{xx}^*}{\partial x^*} + \frac{1}{\rho^*} \frac{\partial \tau_{xy}^*}{\partial y^*} + g_x^*, \quad (2.2)$$

$$\frac{\partial v^*}{\partial t^*} + u^* \frac{\partial v^*}{\partial x^*} + v^* \frac{\partial v^*}{\partial y^*} = -\frac{1}{\rho^*} \frac{\partial p^*}{\partial y^*} + \frac{1}{\rho^*} \frac{\partial \tau_{yx}^*}{\partial x^*} + \frac{1}{\rho^*} \frac{\partial \tau_{yy}^*}{\partial y^*} + g_y^*, \quad (2.3)$$

respectively, where $u^*(x^*, y^*, t^*)$, $v^*(x^*, y^*, t^*)$ denote the velocity in x^* - and y^* -direction, respectively, t^* time, ρ^* density, $p^*(x^*, y^*, t^*)$ pressure, g_j^* the body force per unit mass in j -direction, and $\tau_{jk}^*(x^*, y^*, t^*)$ component jk of the stress tensor $\overline{\overline{\tau^*}}(x^*, y^*, t^*)$.

For a non-Newtonian power-law fluid [12], the stress tensor $\overline{\overline{\tau^*}}$ is given by

$$\overline{\overline{\tau^*}} = K^* |\overline{\overline{e^*}}|^{n-1} \overline{\overline{e^*}}, \quad (2.4)$$

where K^* is a constant, n the power-law index, and $\overline{\overline{e^*}}$ the rate of strain tensor

given by

$$\overline{\overline{e^*}} = \begin{pmatrix} \frac{\partial u^*}{\partial x^*} & \frac{1}{2} \left(\frac{\partial u^*}{\partial y^*} + \frac{\partial v^*}{\partial x^*} \right) \\ \frac{1}{2} \left(\frac{\partial u^*}{\partial y^*} + \frac{\partial v^*}{\partial x^*} \right) & \frac{\partial v^*}{\partial y^*} \end{pmatrix}. \quad (2.5)$$

The matrix norm of $\overline{\overline{e^*}}$, denoted by $|\overline{\overline{e^*}}|$, is (here) equivalent to the largest eigenvalue of $\overline{\overline{e^*}}$. Upon entering the largest eigenvalue of $\overline{\overline{e^*}}$ in (2.4), one obtains for the stress tensor

$$\overline{\overline{\tau^*}} = 2k^* \left[2 \left(\frac{\partial u^*}{\partial x^*} \right)^2 + \left(\frac{\partial u^*}{\partial y^*} + \frac{\partial v^*}{\partial x^*} \right)^2 + 2 \left(\frac{\partial v^*}{\partial y^*} \right)^2 \right]^{\frac{n-1}{2}} \overline{\overline{e^*}}, \quad (2.6)$$

where the constant k^* is defined by $k^* = \left(\frac{1}{2}\right)^n K^*$. The equations for a Newtonian fluid are obtained by setting $n = 1$ and $k^* = \mu^*$, with μ^* the dynamic viscosity.

The Navier-Stokes equations are non-dimensionalized using a reference length L_{ref}^* , velocity U_{ref}^* , density ρ_{ref}^* , viscosity μ_{ref}^* and gravitational constant g_0^* . Then the non-dimensionalized form of the Navier-Stokes equation becomes

$$\frac{\partial u}{\partial x} + \frac{\partial v}{\partial y} = 0, \quad (2.7)$$

$$\frac{\partial u}{\partial t} + u \frac{\partial u}{\partial x} + v \frac{\partial u}{\partial y} = -\frac{1}{r} \frac{\partial p}{\partial x} + \frac{1}{r} \left(\frac{\partial \tau_{xx}}{\partial x} + \frac{\partial \tau_{xy}}{\partial y} \right) + Fr^{-2} g_x, \quad (2.8)$$

$$\frac{\partial v}{\partial t} + u \frac{\partial v}{\partial x} + v \frac{\partial v}{\partial y} = -\frac{1}{r} \frac{\partial p}{\partial y} + \frac{1}{r} \left(\frac{\partial \tau_{yx}}{\partial x} + \frac{\partial \tau_{yy}}{\partial y} \right) + Fr^{-2} g_y, \quad (2.9)$$

where the stress tensor is given by (2.6) after dropping the stars and replacing k^* by $\frac{m}{Re}$, the viscosity ratio over the Reynolds number. Time is made dimensionless with $L_{\text{ref}}^*/U_{\text{ref}}^*$ instead of introducing a separate time scale. A Reynolds number Re , density ratio r , viscosity ratio m and Froude number Fr are introduced according to

$$Re = \frac{\rho_{\text{ref}}^* U_{\text{ref}}^* L_{\text{ref}}^*}{\mu_{\text{ref}}^*}, \quad (2.10)$$

$$r = \frac{\rho^*}{\rho_{\text{ref}}^*}, \quad (2.11)$$

$$m = \frac{k^*}{\mu_{\text{ref}}^*} \left(\frac{U_{\text{ref}}^*}{L_{\text{ref}}^*} \right)^{n-1}, \quad (2.12)$$

$$Fr = \frac{U_{\text{ref}}^*}{\sqrt{g_0^* L_{\text{ref}}^*}}. \quad (2.13)$$

2.2 Orr-Sommerfeld for power-law fluids

The solution of the Navier-Stokes equations is split in a primary (basic) solution and a secondary (perturbed) solution assuming that the latter is a order of magnitude smaller than the former. Further, the primary solution is assumed to be steady, the primary velocity component in x -direction to be only a function of y and the other primary velocity component to be zero. One gets after denoting the primary solution by capital symbols and the secondary solution by tildes

$$u(x, y, t) = U(y) + \tilde{u}(x, y, t), \quad (2.14)$$

$$v(x, y, t) = \tilde{v}(x, y, t), \quad (2.15)$$

$$p(x, y, t) = P(x, y) + \tilde{p}(x, y, t). \quad (2.16)$$

Upon entering the decomposition of the velocity components and pressure in the Navier-Stokes equations, splitting the equations in a zeroth-order (primary flow) and a first order part (the perturbations), one gets for the zeroth-order terms, where the continuity equation is automatically satisfied,

$$0 = -\frac{1}{r} \frac{\partial P}{\partial x} + \frac{m}{Rer} \frac{d}{dy} \left(\frac{dU}{dy} \right)^n + Fr^{-2} g_x, \quad (2.17)$$

$$0 = -\frac{1}{r} \frac{\partial P}{\partial y} + Fr^{-2} g_y, \quad (2.18)$$

which govern the primary flow. For the first-order terms one finds

$$\frac{\partial \tilde{u}}{\partial x} + \frac{\partial \tilde{v}}{\partial y} = 0, \quad (2.19)$$

$$\begin{aligned} \frac{\partial \tilde{u}}{\partial t} + U \frac{\partial \tilde{u}}{\partial x} + \tilde{v} \frac{dU}{dy} &= -\frac{1}{r} \frac{\partial \tilde{p}}{\partial x} + 2 \frac{m}{Rer} \left(\frac{dU}{dy} \right)^{n-1} \frac{\partial^2 \tilde{u}}{\partial x^2} \\ &\quad + \frac{mn}{Rer} \frac{\partial}{\partial y} \left(\left(\frac{dU}{dy} \right)^{n-1} \left(\frac{\partial \tilde{u}}{\partial y} + \frac{\partial \tilde{v}}{\partial x} \right) \right), \end{aligned} \quad (2.20)$$

$$\begin{aligned} \frac{\partial \tilde{v}}{\partial t} + U \frac{\partial \tilde{v}}{\partial x} &= -\frac{1}{r} \frac{\partial \tilde{p}}{\partial y} + \frac{mn}{Rer} \left(\frac{dU}{dy} \right)^{n-1} \frac{\partial}{\partial x} \left(\frac{\partial \tilde{u}}{\partial y} + \frac{\partial \tilde{v}}{\partial x} \right) \\ &\quad + 2 \frac{m}{Rer} \frac{\partial}{\partial y} \left(\left(\frac{dU}{dy} \right)^{n-1} \frac{\partial \tilde{v}}{\partial y} \right), \end{aligned} \quad (2.21)$$

which, for a known primary flow solution, governs the secondary flow.

To satisfy the continuity equation for the secondary flow, a stream function $\tilde{\Phi}$ is introduced, according to

$$\tilde{u}(x, y, t) = \frac{\partial \tilde{\Phi}}{\partial y}(x, y, t), \quad (2.22)$$

$$\tilde{v}(x, y, t) = -\frac{\partial \tilde{\Phi}}{\partial x}(x, y, t). \quad (2.23)$$

The resulting equations are linear in the stream function $\tilde{\Phi}$ and the pressure \tilde{p} permitting the normal mode solutions

$$\tilde{\Phi}(x, y, t) = \phi(y)e^{i\alpha(x-ct)} = \phi(y)e^{i(\alpha x - \omega t)}, \quad (2.24)$$

$$\tilde{p}(x, y, t) = f(y)e^{i\alpha(x-ct)} = f(y)e^{i(\alpha x - \omega t)}, \quad (2.25)$$

where $i^2 = -1$, α the wave number and c the wave speed, both complex, just as the eigenfunctions $\phi(y)$ and $f(y)$. The frequency ω equals αc . It is assumed that α and c in both $\tilde{\Phi}$ and \tilde{p} are equal, i.e., interactions between different normal modes will not be considered. It is a matter of convenience to work with complex normal modes. The physical solutions are obtained by taking the real parts of (2.24) and (2.25).

In general both α and c are complex. A temporal stability analysis is obtained by assuming α real while for a spatial stability analysis c is taken to be real. From this point on, α is taken real (temporal analysis) and greater than zero, related to the (non-dimensional) wave length λ by

$$\alpha = \frac{2\pi}{\lambda}. \quad (2.26)$$

A flow is said to be stable, if for all wave numbers α , the solution of the Navier-Stokes equations for the secondary flow given by (2.19)-(2.21) possess imaginary parts of c less than zero. In all other cases, the flow is said to be (linearly) unstable. This is easily shown by writing c as $c = c_r + ic_i$, so that $e^{i\alpha(x-ct)} = e^{\alpha c_i t} e^{i\alpha(x-c_r t)}$ indicating exponential growth for positive c_i and exponential decay for negative c_i .

Upon substitution of the normal mode form of the stream function and the pressure in the Navier-Stokes equations for the secondary flow, and division by $e^{i\alpha(x-ct)}$, one gets from equations (2.20) and (2.21)

$$-(U - c)\phi' + U'\phi = \frac{1}{r}f - \frac{m(U')^{n-1}}{i\alpha Rer} (n\phi''' + (n-2)\alpha^2\phi') - \frac{m(U')^{n-2}U''}{i\alpha Rer} n(n-1) (\phi'' + \alpha^2\phi), \quad (2.27)$$

$$(U - c)\alpha^2\phi = -\frac{1}{r}f' + \frac{i\alpha m(U')^{n-1}}{Rer} ((n-2)\phi'' + n\alpha^2\phi) - 2\frac{i\alpha m(U')^{n-2}U''}{Rer} (n-1)\phi', \quad (2.28)$$

where a prime indicates differentiation with respect to y .

Elimination of the pressure term from above two equations yields the Orr-Sommerfeld equation for power-law fluids

$$\begin{aligned} & \phi'''' - 2\alpha^2\phi'' + \alpha^4\phi - \frac{i\alpha Rer}{mn(U')^{n-1}} [(U - c)(\phi'' - \alpha^2\phi) - U''\phi] \\ & + (n-1) \left[2\frac{U''}{U'}\phi''' + \left((n-2) \left(\frac{U''}{U'} \right)^2 + \frac{U'''}{U'} + \frac{4\alpha^2}{n} \right) \phi'' \right] \\ & + (n-1)\alpha^2 \left[2\frac{n-2}{n}\frac{U''}{U'}\phi' + \left(\frac{U'''}{U'} + (n-2) \left(\frac{U''}{U'} \right)^2 \right) \phi \right] = 0. \end{aligned} \quad (2.29)$$

For a Newtonian fluid ($n = 1$), the Orr-Sommerfeld equation reduces to

$$\phi'''' - 2\alpha^2\phi'' + \alpha^4\phi - \frac{i\alpha Rer}{m} [(U - c)(\phi'' - \alpha^2\phi) - U''\phi] = 0. \quad (2.30)$$

2.3 Power-law fluid sheared by Blasius flow

The problem considered consists of the stability of a thin layer of fluid sheared by a stream of air (another fluid). The main application, here, is the air flow over a wing covered with de- or anti-icing fluid. Consider as a generic model of this application, two infinite parallel horizontal fluid layers on top of each other with the lower one bounded by a fixed wall and the upper one stretching to infinity (see figure 2.1). The upper fluid (layer one) is assumed to be Newtonian, while the lower fluid layer (layer two) can have a Newtonian or a power-law fluid behaviour. A coordinate system is introduced with the

y -axis normal to the wall and the x -axis along the interface of both fluid layers. The positive directions are indicated in figure 2.1. Gravity is assumed to act in the negative y -direction, i.e. $g_x = 0$ and $g_y = 1$. The wall is indicated by $y = y_w < 0$.

The (linear temporal) stability of this configuration is studied by superposing small perturbations to the steady primary solution as discussed in the previous section. The assumption of a steady, parallel primary flow in x -direction bounded by a wall at $y = y_w$ together with the no-slip condition causes the primary flow to be described by $U = U(y)$ and $V = 0$ (i.e. (2.17) - (2.18)).

The upper layer will be referred to with a subscript 1 and the lower layer with a subscript 2, except for the (amplitude of the) stream function which is denoted by ϕ in the upper and by χ in the lower layer. The reference quantities are chosen as $U_{\text{ref}}^* = U_{\infty}^*$, the (undisturbed) velocity at infinity, $\rho_{\text{ref}}^* = \rho_1^*$, the density of the upper layer and $\mu_{\text{ref}}^* = \mu_1^*$, the viscosity of the upper layer. A reference length will be chosen later. This choice makes m and r equal to unity in the upper layer. Furthermore, n is also equal to one for the upper layer, because of the Newtonian character of air. As a consequence, the subscript 2 of m , n and r will be omitted.

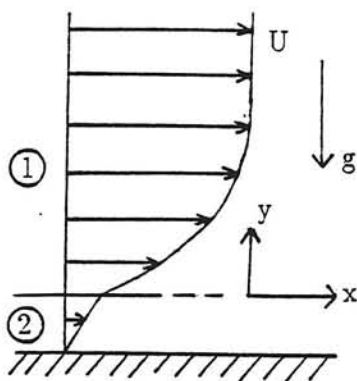


FIGURE 2.1: Two-layer flow configuration

The fourth-order linear Orr-Sommerfeld differential equation, given by (2.30) for the upper layer and (2.29) for the lower layer are complemented with boundary and interface conditions in order to complete the description of the stability problem. There are the no-slip boundary condition at the wall $y = y_w$, and continuity of velocity and stress in both directions at the interface $y = 0$, and the velocity components have to vanish when y goes to infinity, i.e., in total 8 conditions.

2.4 No-slip at the wall

The no-slip condition at the wall $y = y_w$ can be written as,

$$u_2(x, y_w, t) = U_2(y_w) + \tilde{u}_2(x, y_w, t) = 0, \quad (2.31)$$

$$v_2(x, y_w, t) = \tilde{v}_2(x, y_w, t) = 0. \quad (2.32)$$

Splitting above equations in a zeroth-order and first-order part yields for the zeroth-order part

$$U_2(y_w) = 0, \quad (2.33)$$

and for the first-order part

$$\tilde{u}_2(x, y_w, t) = \chi'(y_w)e^{i\alpha(x-ct)} = 0, \quad (2.34)$$

$$\tilde{v}_2(x, y_w, t) = -i\alpha\chi(y_w)e^{i\alpha(x-ct)} = 0. \quad (2.35)$$

The latter two equations can be reduced to

$$\chi'(y_w) = 0, \quad (2.36)$$

$$\chi(y_w) = 0. \quad (2.37)$$

2.5 Location of the interface

The difference between the actual location of the interface and that of the interface between the zeroth-order solution for the two fluids ($y = 0$) is indicated by $\eta(x, t)$, with η assumed to be of the same order of magnitude and having the same normal form as the velocity and pressure perturbations, and it is written as

$$\eta(x, t) = Ce^{i\alpha(x-ct)}, \quad (2.38)$$

where C is a complex constant.

Using the kinematic condition, the velocity in y -direction at the interface can be written as

$$v(x, \eta(x, t), t) = \frac{d\eta(x, t)}{dt} = u(x, \eta(x, t), t) \frac{\partial \eta}{\partial x} + \frac{\partial \eta}{\partial t}. \quad (2.39)$$

Substitution of (2.38) in the above equation, substitution of the stream function of the upper (or lower fluid layer) and linearization around $y = 0$ yields

for the location of the interface

$$\eta(x, t) = \frac{\phi(0^+)}{c - U_1(0^+)} e^{i\alpha(x-ct)} \left(= \frac{\chi(0^-)}{c - U_2(0^-)} e^{i\alpha(x-ct)} \right). \quad (2.40)$$

So, from the kinematic interface condition, one finds the amplitude of the interface perturbation.

2.6 Continuity of velocity

Continuity of the x -component of the velocity can be expressed as,

$$u_1(x, \eta(x, t)^+, t) = u_2(x, \eta(x, t)^-, t), \quad (2.41)$$

which can be split in

$$U_1(\eta(x, t)^+) + \tilde{u}_1(x, \eta(x, t)^+, t) = U_2(\eta(x, t)^-) + \tilde{u}_2(x, \eta(x, t)^-, t). \quad (2.42)$$

Upon performing a Taylor expansion around $y = 0$, and splitting the equation in a zeroth-order and first-order part, one gets for the primary flow

$$U_1(0^+) = U_2(0^-), \quad (2.43)$$

and for the secondary flow

$$\phi'(0^+) - \chi'(0^-) = \frac{\phi(0^+)}{c - U_1(0^+)} (U_2'(0^-) - U_1'(0^+)). \quad (2.44)$$

Now, consider continuity of the y -component of the velocity, stated by

$$v_1(x, \eta(x, t)^+, t) = v_2(x, \eta(x, t)^-, t), \quad (2.45)$$

which to first-order accuracy is equivalent to

$$\tilde{v}_1(x, \eta(x, t)^+, t) = \tilde{v}_2(x, \eta(x, t)^-, t), \quad (2.46)$$

using that there is no primary component in y -direction. In the same way, as for the continuity of the x -component of the velocity, one obtains

$$\phi(0^+) = \chi(0^-). \quad (2.47)$$

2.7 Dynamic boundary conditions

In an incompressible flow of a power-law fluid, the (dimensionless) two-dimensional total stress tensor ($\bar{\sigma}$, components σ_{jk}) can be written as

$$\sigma_{jk} = -p\delta_{jk} + \tau_{jk}, \quad (2.48)$$

where τ_{jk} is the non-dimensional form of (2.4) and δ_{jk} is the Kronecker delta equal to one for $j = k$, otherwise equal to zero. The components of the total stress vector on an arbitrary surface with unit normal vector \vec{n} (see fig. (2.2)) are given by

$$\vec{s} = \bar{\sigma} \cdot \vec{n}. \quad (2.49)$$

The unit tangential vector \vec{t} and the unit normal vector \vec{n} on the interface are given by

$$\vec{t} = \frac{\vec{e}_x + \frac{\partial n}{\partial x} \vec{e}_y}{\sqrt{1 + \left(\frac{\partial n}{\partial x}\right)^2}} = n_y \vec{e}_x - n_x \vec{e}_y, \quad (2.50)$$

$$\vec{n} = \frac{-\frac{\partial n}{\partial x} \vec{e}_x + \vec{e}_y}{\sqrt{1 + \left(\frac{\partial n}{\partial x}\right)^2}} = n_x \vec{e}_x + n_y \vec{e}_y, \quad (2.51)$$

where \vec{e}_x and \vec{e}_y are the unit vectors in the x - and y -direction, respectively.

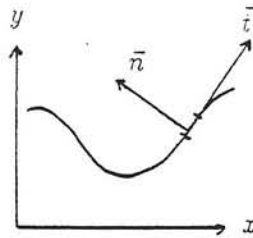


FIGURE 2.2: Definition of normal and tangential (unit) vector

Now, the tangential component s_t of the total stress vector \vec{s} is given by

$$s_t = \vec{s} \cdot \vec{t} = \sigma_{xx} n_x n_y + \sigma_{xy} (n_y^2 - n_x^2) - \sigma_{yy} n_x n_y, \quad (2.52)$$

the inner vector product of \vec{s} and \vec{t} . For the normal component s_n , one can derive

$$s_n = \vec{s} \cdot \vec{n} = \sigma_{xx} n_x^2 + 2\sigma_{xy} n_x n_y + \sigma_{yy} n_y^2. \quad (2.53)$$

To obtain continuity of shear stress, the shear stress just above the interface has to equal the shear stress just below the interface, leading to

$$s_{t1}(x, \eta(x, t)^+, t) = s_{t2}(x, \eta(x, t)^-, t), \quad (2.54)$$

where it has been used that the (constant) interfacial surface tension to first order approximation does not have a resulting component in tangential direction. The above equation can be split in a zeroth- and first-order condition after performing a Taylor approximation around $y = 0$. One obtains

$$U_1'(0^+) = m (U_2'(0^-))^n \quad (2.55)$$

for the primary flow and

$$\begin{aligned} \phi''(0^+) + \alpha^2 \phi(0^+) &= mn (U_2'(0^-))^{n-1} (\chi''(0^-) + \alpha^2 \chi(0^-)) \\ &+ \frac{\phi(0^+)}{c - U_1(0^+)} \left(mn (U_2'(0^-))^{n-1} U_2''(0^-) - U_1''(0^+) \right) \end{aligned} \quad (2.56)$$

for the secondary flow.

The normal stress just above and below the interface is in equilibrium with the normal component of surface tension to give, to first-order approximation

$$s_{n1}(x, \eta(x, t)^+, t) - s_{n2}(x, \eta(x, t)^-, t) + S_n(x, \eta(x, t), t) = 0, \quad (2.57)$$

where S_n is the contribution of the surface tension in normal direction given by (see for example [20])

$$S_n = \frac{We \eta_{xx}}{\sqrt{(1 + \eta_x^2)^3}}, \quad (2.58)$$

where the Weber number We is defined as

$$We = \frac{T^*}{\rho_{\text{ref}}^* U_{\text{ref}}^{*2} L_{\text{ref}}^*}, \quad (2.59)$$

where T^* is the surface tension. As before, one obtains the condition for the primary flow and the one for the perturbation by splitting the flow variables

in a zeroth-order part and a first-order perturbation and performing a Taylor approximation around $y = 0$. For the primary flow, one gets

$$P_1(x, 0^+) = P_2(x, 0^-) \quad (2.60)$$

and for the perturbations after elimination of the pressure using (2.27)

$$\begin{aligned} m \left(U_2'(0^-) \right)^{n-1} \left(n \chi'''(0^-) + (n-4) \alpha^2 \chi'(0^-) \right) - \left(\phi'''(0^+) - 3 \alpha^2 \phi'(0^+) \right) \\ + i \alpha Re r \left[(c - U_1(0^+)) \chi'(0^-) + U_2'(0^-) \chi(0^-) \right] \\ - i \alpha Re \left[(c - U_1(0^+)) \phi'(0^+) + U_1'(0^+) \phi(0^+) \right] \\ + m \left(U_2'(0^-) \right)^{n-2} U_2''(0^-) n(n-1) \left(\chi''(0^-) + \alpha^2 \chi(0^-) \right) \quad (2.61) \\ - i \alpha Re \frac{\phi(0^+)}{c - U_1(0^+)} \left(P_1'(0^+) - P_2'(0^-) + \alpha^2 We \right) = 0. \end{aligned}$$

Özgen [29] derived a similar set of equations for non-Newtonian power-law fluids only assuming that $U_2''(0^-) = 0$, which is the case for Blasius flow. His equations are identical to the ones given in this report, except for equation (2.61) in this report and equation (96) in his report. Özgen's result can be obtained after setting $n = 1$ (and $U_2''(0^-) = 0$) in equation (2.61).

2.8 Conditions at infinity

At infinity, the primary velocity components have to reach the undisturbed free stream given by

$$U \rightarrow 1, \quad \text{as } y \rightarrow \infty, \quad (2.62)$$

$$V \rightarrow 0, \quad \text{as } y \rightarrow \infty, \quad (2.63)$$

and the disturbed velocity components have to vanish which can be mathematically stated as,

$$\chi(y) \rightarrow 0, \quad \text{as } y \rightarrow \infty, \quad (2.64)$$

$$\chi'(y) \rightarrow 0, \quad \text{as } y \rightarrow \infty. \quad (2.65)$$

2.9 Energy

The (mechanical) energy distribution of the disturbances throughout the flow field can be computed by calculating the inner product of the perturbed velocities and the first-order momentum equations in x - and y -direction and averaging this result over one wave length $\lambda = \frac{2\pi}{\alpha}$. For a power law fluid, one obtains

$$\frac{dE}{dt} = RS + PR + DI, \quad (2.66)$$

where E is the kinetic energy of the disturbances given by

$$E = \frac{1}{2\lambda} \int_0^\lambda (\tilde{u}^2 + \tilde{v}^2) dx, \quad (2.67)$$

RS the Reynolds stress term exhibiting the interaction between the primary flow and the secondary velocity components given by,

$$RS = \frac{1}{\lambda} \frac{dU}{dy} \int_0^\lambda (-\tilde{u}\tilde{v}) dx, \quad (2.68)$$

PR the pressure term originating from the interaction between the disturbances in the pressure and velocity, given by

$$PR = -\frac{1}{\lambda r} \int_0^\lambda \left(\tilde{u} \frac{\partial \tilde{p}}{\partial x} + \tilde{v} \frac{\partial \tilde{p}}{\partial y} \right) dx, \quad (2.69)$$

and, finally, DI indicates the effect of the viscous forces given by

$$\begin{aligned} DI = & \frac{m(U')^{n-1}}{\lambda Rer} \int_0^\lambda \left[(2-n)\tilde{u} \frac{\partial^2 \tilde{u}}{\partial x^2} + n\tilde{u} \frac{\partial^2 \tilde{u}}{\partial y^2} \right] dx \\ & + \frac{m(U')^{n-1}}{\lambda Rer} \int_0^\lambda \left[n\tilde{v} \frac{\partial^2 \tilde{v}}{\partial x^2} + (2-n)\tilde{v} \frac{\partial^2 \tilde{v}}{\partial y^2} \right] dx \\ & + \frac{m(n-1)(U')^{n-1} U''}{\lambda Rer} \int_0^\lambda \left[n\tilde{u} \left(\frac{\partial \tilde{u}}{\partial y} + \frac{\partial \tilde{v}}{\partial x} \right) + 2\tilde{v} \frac{\partial \tilde{v}}{\partial y} \right] dx. \end{aligned} \quad (2.70)$$

These relations can be used for the lower fluid layer after adding a subscript 2 to \tilde{u} , \tilde{v} and \tilde{p} and for the upper fluid layer after adding a subscript 1 and setting

m , n and r equal to unity. Upon substitution of the real parts of the normal mode forms of the unknown quantities and integration, the resulting equations are used to compute the energy distribution numerically. These equations are after setting $t = 0$

$$\frac{dE}{dt} = \frac{\pi c_i}{\lambda} [\alpha^2 (\phi_r^2 + \phi_i^2) + \phi_r'^2 + \phi_i'^2], \quad (2.71)$$

$$RS = \frac{\pi}{\lambda} \frac{dU}{dy} [\phi_r \phi_i' - \phi_i \phi_r'], \quad (2.72)$$

$$PR = \frac{\pi}{\lambda r} [\phi_r f_i' + \phi_r' f_i - \phi_i f_r' - \phi_i' f_r], \quad (2.73)$$

$$DI = \frac{m(U')^{n-1}}{2Re_r} [(n-2)\alpha^2 (\phi_r'^2 + \phi_i'^2 - \phi_r \phi_r'' - \phi_i \phi_i'')] \\ + \frac{m(U')^{n-1}}{2Re_r} [n(\phi_r' \phi_r''' + \phi_i' \phi_i''') - n\alpha^4 (\phi_r^2 + \phi_i^2)], \quad (2.74)$$

where it has been used that either $U'' = 0$ or $n = 1$.

In a global sense, the origin of the change in kinetic energy is obtained by integrating equation (2.66) from the wall to infinity, where below the interface the energy distribution for the lower layer has to be used and above the one for the upper layer. One obtains (using a subscript t to indicate integration over y from y_w to infinity)

$$\frac{dE_t}{dt} = RS_t + PR_t + DI_t, \quad (2.75)$$

where E_t and RS_t follow from (2.67) and (2.68), respectively. Further, for the pressure term, one finds using Stokes' integral theorem, the no-slip conditions at the wall and that the disturbances disappear for $y \rightarrow \infty$

$$PR_t = -\frac{1}{\lambda r} \int_0^\lambda (\tilde{p}_2 \tilde{v}_2)|_{y=0-} dx + \frac{1}{\lambda} \int_0^\lambda (\tilde{p}_1 \tilde{v}_1)|_{y=0+} dx. \quad (2.76)$$

In case of a Newtonian fluid (i.e. the upper fluid layer), the dissipation term (DI_{t1}) can be written, after partial integration, as

$$DI_{t1} = -\frac{1}{\lambda Re} \int_0^\lambda \left[\tilde{u}_1 \left(\frac{\partial \tilde{u}_1}{\partial y} - \frac{\partial \tilde{v}_1}{\partial x} \right) \right] \Big|_{y=0+} dx \\ - \frac{1}{\lambda Re} \int_0^\infty \int_0^\lambda \left(\frac{\partial \tilde{u}_1}{\partial y} - \frac{\partial \tilde{v}_1}{\partial x} \right)^2 dx dy, \quad (2.77)$$

where the integrands involve the perturbation vorticity $\tilde{\omega} = \frac{\partial \tilde{v}}{\partial x} - \frac{\partial \tilde{u}}{\partial y}$.

2.10 Vorticity/enstrophy

Vorticity is defined as the curl of the velocity field. For two-dimensional problems, the vorticity is given by

$$\omega = \frac{\partial v}{\partial x} - \frac{\partial u}{\partial y}, \quad (2.78)$$

which can be split in a vorticity for the primary flow given by (2.78) upon replacing ω , v and u by their respective capital character and for the secondary flow by the same equation after adding tildes to ω , v and u . The equation for the distribution of the enstrophy, i.e. $\tilde{\omega}^2$, the vorticity squared, is obtained by multiplying the secondary vorticity with the curl of the secondary momentum equations, and averaging the result over one wave length. Using the same terms as for the energy distribution (E , RS , PR and DI) have been used after adding a subscript v , the result can be written as

$$\frac{dE_v}{dt} = RS_v + PR_v + DI_v, \quad (2.79)$$

where the following definitions have been used

$$E_v = \frac{1}{2\lambda} \int_0^\lambda \tilde{\omega}^2 dx, \quad (2.80)$$

$$RS_v = \frac{1}{\lambda} \frac{d^2 U}{dy^2} \int_0^\lambda \tilde{v} \tilde{\omega} dx, \quad (2.81)$$

$$PR_v = 0, \quad (2.82)$$

$$\begin{aligned} DI_v = & \frac{mn(U')^{n-1}}{\lambda Rer} \int_0^\lambda \left[\tilde{\omega} \left(\frac{\partial^2 \tilde{\omega}}{\partial x^2} + \frac{\partial^2 \tilde{\omega}}{\partial y^2} \right) \right] dx \\ & + \frac{2m(n-1)(U')^{n-1}}{\lambda Rer} \int_0^\lambda \left[\tilde{\omega} \left(\frac{\partial^3 \tilde{u}}{\partial x^2 \partial y} - \frac{\partial^3 \tilde{v}}{\partial x \partial y^2} \right) \right] dx \\ & + \frac{2m(n-1)(U')^{n-2} U''}{\lambda Rer} \int_0^\lambda \tilde{\omega} \left(\frac{\partial^2 \tilde{v}}{\partial x \partial y} - \frac{\partial^2 \tilde{u}}{\partial x^2} - n \frac{\partial^2 \tilde{u}}{\partial y^2} - n \frac{\partial^2 \tilde{v}}{\partial x \partial y} \right) dx \\ & - \frac{mn(n-1)(U')^{n-1}}{\lambda Rer} \left[(n-2) \left(\frac{U''}{U'} \right)^2 + \left(\frac{U'''}{U'} \right) \right] \int_0^\lambda \tilde{\omega} \left(\frac{\partial \tilde{u}}{\partial y} + \frac{\partial \tilde{v}}{\partial x} \right) dx. \end{aligned} \quad (2.83)$$

A subscript 1 or 2 should be added to indicate fluid layer one or fluid layer two, respectively. For the upper layer, one also has to set m , n and r equal to unity. Upon substitution of the real parts of the perturbation quantities in the enstrophy equation, one can derive the following expressions for the enstrophy distribution according to the ones for the energy distribution after setting $t = 0$

$$\frac{dE_v}{dt} = \frac{\pi c_i}{\lambda} \left[\alpha^4 (\phi_r^2 + \phi_i^2) - 2\alpha^2 (\phi_r \phi_r'' + \phi_i \phi_i'') + \phi_r''^2 + \phi_i''^2 \right], \quad (2.84)$$

$$RS_v = \frac{\pi}{\lambda} \frac{d^2 U}{dy^2} [\phi_r \phi_i'' - \phi_i \phi_r''], \quad (2.85)$$

$$DI_v = \frac{m (U')^{n-1}}{2Re_r} \left[2(n-2)\alpha^2 (\phi_r''^2 + \phi_i''^2) - n\alpha^2 (\phi_r \phi_r'''' + \phi_i \phi_i''') \right] \\ + \frac{m (U')^{n-1}}{2Re_r} \left[(4-n)\alpha^4 (\phi_r \phi_r'' + \phi_i \phi_i'') \right] \\ + \frac{m (U')^{n-1}}{2Re_r} \left[n (\phi_r'' \phi_r'''' + \phi_i'' \phi_i''') - n\alpha^6 (\phi_r^2 + \phi_i^2) \right], \quad (2.86)$$

where it has been used that either $U'' = 0$ or $n = 1$.

The equations for the global value of the enstrophy of both layers are obtained after integration of (2.79) over y from the wall to infinity in a manner similar to the case of the energy distribution discussed in the previous section.

2.11 Primary solution

The primary flow has to be a solution of (2.17) and (2.18). Here, g_x is set to zero and g_y to one. According to these equations, $\frac{\partial P}{\partial x}$ cannot be a function of x , nor can $\frac{\partial P}{\partial y}$, since U is only a function of y . Therefore $\frac{\partial P}{\partial x}$ is a constant. After defining

$$A = \frac{Re}{m} \frac{\partial P}{\partial x}, \quad (2.87)$$

the solution of equation (2.17) is found to be

$$U(y) = \frac{1}{A} \frac{n}{n+1} (Ay + B)^{\frac{n+1}{n}} + C \quad (2.88)$$

in case $A \neq 0$, else

$$U(y) = \hat{B}y + \hat{C}, \quad (2.89)$$

where B , C , \hat{B} and \hat{C} are arbitrary constants. The pressure distribution follows from (2.18)

$$P(x, y) = rFr^{-2}y + \frac{\partial P}{\partial x}x + p_0, \quad (2.90)$$

where $\frac{\partial P}{\partial x}$ is constant and p_0 is the pressure in the far field. For a Newtonian fluid, (2.88) reduces to a quadratic profile. In the absence of a pressure gradient in x -direction ($A = 0$) the primary velocity profile is linear (for both Newtonian and non-Newtonian flow).

For the lower layer the primary velocity profile is given by (2.88) or (2.89), while for the upper layer the same expressions are valid with n equal to one. However, Drazin and Reid [9] argue that also other velocity profiles can be used in the linear stability theory as long as their velocity component in y -direction is small compared to the velocity component in x -direction, so-called nearly-parallel flows. Blasius flow is an example of such a flow.

Therefore, Blasius flow is taken as the primary flow for the upper fluid layer. The velocity components in x - and y -direction are given by [33]

$$U_1(x, y) = g'(y), \quad (2.91)$$

$$V_1(x, y) = \frac{1}{2Re}(yg'(y) - g(y)), \quad (2.92)$$

where the function $g(y)$ satisfies

$$g(y)g''(y) + 2g'''(y) = 0, \quad (2.93)$$

with boundary conditions

$$g(y) = 0, \quad y = 0, \quad (2.94)$$

$$g'(y) = 0, \quad y = 0, \quad (2.95)$$

$$g'(y) \rightarrow 1, \quad y \rightarrow \infty, \quad (2.96)$$

where the coordinate y^* is non-dimensionalized by $L_{\text{ref}}^* = \sqrt{\frac{\mu_1^* x^*}{\rho_1^* U_\infty^*}}$, which will be used as reference length. A certain x^* -location is chosen (and hence reference length) and U_1 is considered to be only a function of y and V_1 is neglected.

For mathematical ease, a reference frame moving with the constant primary velocity of the interface is introduced setting $U_1(0^+) = 0$. This Galilean transformation only changes the primary velocity profile.

The constants B , C , \hat{B} and \hat{C} in the primary flow of the lower layer can be obtained using the no-slip condition at the wall (here in the moving frame of reference that the velocity is set equal to zero at the interface), and equation (2.55), continuity of shear stress at the interface, to give

$$B = \frac{U_1'(0^+)}{m}, \quad (2.97)$$

$$C = -\frac{1}{A} \frac{n}{n+1} \left(\frac{U_1'(0^+)}{m} \right)^{\frac{n+1}{n}}, \quad (2.98)$$

$$\hat{B} = \left(\frac{U_1'(0^+)}{m} \right)^{\frac{1}{n}}, \quad (2.99)$$

$$\hat{C} = 0. \quad (2.100)$$

The velocity of the interface, i.e., the velocity at $y = y_w$ then follows from equation (2.88) or (2.89) upon substitution of $y = y_w$.

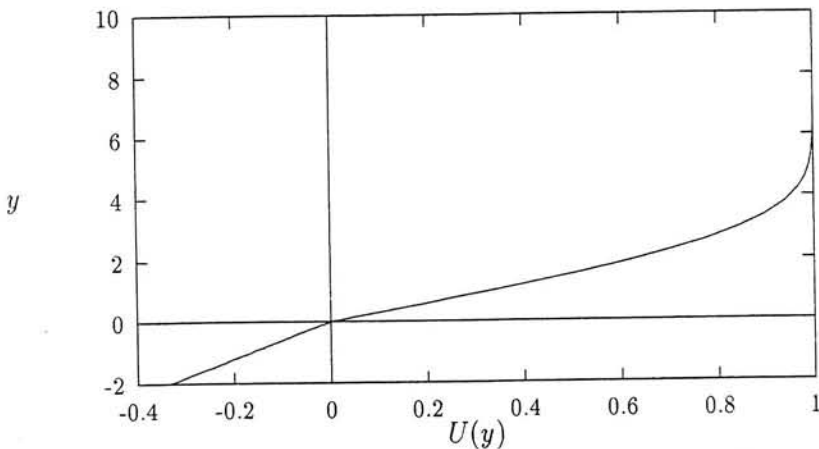


FIGURE 2.3: Primary velocity profile ($y_w = -2, m = 2, n = 1$)

At a certain value of y , say y_i , the so-called virtual interface, the Blasius boundary-layer profile is cut-off and a uniform flow is assumed from hereon towards infinity equal to the free stream velocity (U_∞^*),

$$U(y) = 1, \quad (2.101)$$

In this case, i.e., the case of a uniform flow, the Orr-Sommerfeld equation (2.30) can be written as

$$\psi'''' - (\alpha^2 + \gamma^2)\psi'' + \alpha^2\gamma^2\psi = 0, \quad (2.102)$$

where ϕ has been replaced by ψ and γ^2 is defined by

$$\gamma^2 = \alpha^2 + i\alpha Re(1 - c), \quad \Re(\gamma) > 0. \quad (2.103)$$

The solution of above ordinary differential equation is given by

$$\psi(y) = De^{-\alpha(y-y_i)} + Ee^{-\gamma(y-y_i)}, \quad (2.104)$$

where it has been used that the solution remains bounded for $y \rightarrow \infty$ (therefore is also $\Re(\gamma) > 0$). D and E are arbitrary constants.

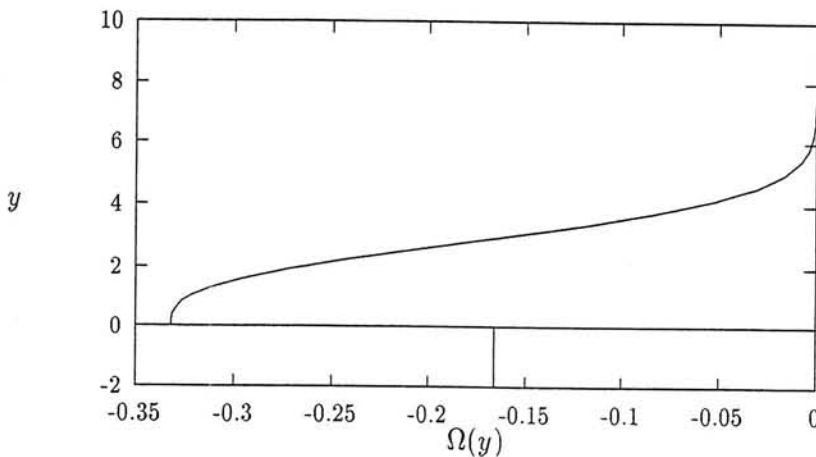


FIGURE 2.4: Primary vorticity distribution ($y_w = -2, m = 2, n = 1$)

At the virtual interface, continuity of velocity and stress in both directions are required, which can be derived from equations (2.44), (2.47), (2.56) and (2.61) after changing χ in ψ , $y = 0$ in $y = y_i$ and setting $n = 1, m = 1, r = 1$ and $We = 0$. After some rearranging, the following four interface conditions are obtained for the virtual interface

$$\phi(y_i^-) = \psi(y_i^+), \quad (2.105)$$

$$\phi'(y_i^-) = \psi'(y_i^+), \quad (2.106)$$

$$\phi''(y_i^-) = \psi''(y_i^+), \quad (2.107)$$

$$\phi'''(y_i^-) = \psi'''(y_i^+). \quad (2.108)$$

Figure 2.3 gives the primary velocity profile and figure 2.4 the primary vorticity distribution of a Newtonian fluid in the lower layer using a viscosity ratio of

2 and assuming the solid wall at $y_w = -2$. For convenience, the interface velocity is set equal to zero. Clearly, one recognizes the Blasius profile in the upper fluid layer. The boundary-layer ends at about $y = 6$ and starts linearly at the fluid interface. The difference in viscosity causes the discontinuity of the first derivative of the velocity profile and therewith the jump in the vorticity distribution. It should be noted that for air/water or air/anti-icing systems, the viscosity ratio is fairly high ($60 - 10^5$) resulting in a very small primary velocity component in the lower fluid layer and a vorticity almost equal to zero.

Chapter 3

Numerical analysis

This chapter describes the numerical algorithm used to calculate the eigenvalues of the linear stability problem derived in the previous chapter. A spectral collocation method based on Chebyshev polynomials is used to discretize the equations. The resulting algebraic eigenvalue problem is solved using a QZ-algorithm.

3.1 Chebyshev polynomials

The m -th Chebyshev polynomial of the first kind is defined by

$$T_m(x) = \cos(m \arccos(x)), \quad (3.1)$$

for x between $[-1, 1]$ and $m = 0, 1, 2, \dots$, which are the eigenfunctions of the singular Sturm-Liouville problem

$$\left(\sqrt{1-x^2}T_m'(x)\right)' + \frac{m^2}{\sqrt{1-x^2}}T_m(x) = 0, \quad (3.2)$$

accompanied by the boundary condition $T_m(1) = 1$ [7]. Figure (3.1) gives a picture of several Chebyshev polynomials. The Chebyshev polynomials can be expressed recursively as,

$$T_0(x) = 1, \quad (3.3)$$

$$T_1(x) = x, \quad (3.4)$$

and

$$T_m(x) = 2xT_{m-1}(x) - T_{m-2}(x), \quad \text{for } m = 2, 3, \dots, \quad (3.5)$$

or as a power series as

$$T_m(x) = \frac{m}{2} \sum_{i=0}^{[m/2]} (-1)^i \frac{(m-i-1)!}{i!(m-2i)!} (2x)^{m-2i}, \quad (3.6)$$

where $[m/2]$ denotes the integral part of $m/2$. Interesting properties of the orthogonal Chebyshev polynomials are

$$|T_m(x)| \leq 1, \quad (3.7)$$

$$T_m(\pm 1) = (\pm 1)^m, \quad (3.8)$$

$$\int_{-1}^1 \frac{T_m^2(x)}{\sqrt{1-x^2}} dx = c_m \frac{\pi}{2}, \quad (3.9)$$

where

$$c_m = \begin{cases} 2, & \text{if } m = 0 \\ 1, & \text{if } m \geq 1 \end{cases} \quad (3.10)$$

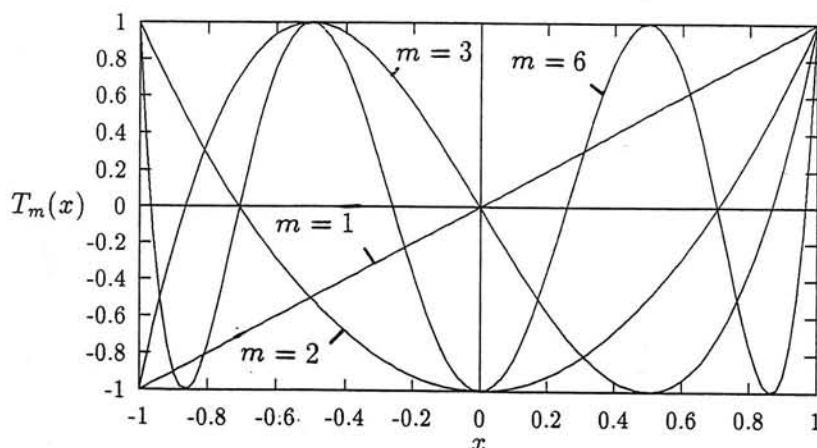


FIGURE 3.1: m -th Chebyshev polynomial for $m = 1, 2, 3$ and 6

A function $v(x)$ defined in the interval $-1 \leq x \leq 1$ can be expanded in a series of Chebyshev polynomials as

$$v(x) = \sum_{m=0}^{\infty} a_m T_m(x), \quad (3.11)$$

where

$$a_m = \frac{2}{\pi c_m} \int_{-1}^1 \frac{v(x)T_m(x)}{\sqrt{1-x^2}} dx. \quad (3.12)$$

For the numerical implementation, one will need the derivatives of the Chebyshev polynomials up to order four. These derivatives can be easily found by differentiating (3.1) to give (for $x \neq \pm 1$)

$$T'_m(x) = \frac{\sin(m \arccos(x))m}{\sqrt{1-x^2}}, \quad (3.13)$$

$$T''_m(x) = -\frac{\cos(m \arccos(x))m^2}{1-x^2} + \frac{\sin(m \arccos(x))mx}{(1-x^2)^{3/2}}, \quad (3.14)$$

$$T'''_m(x) = -\frac{\sin(m \arccos(x))m^3}{(1-x^2)^{3/2}} - 3\frac{\cos(m \arccos(x))m^2x}{(1-x^2)^2} + 3\frac{\sin(m \arccos(x))mx^2}{(1-x^2)^{5/2}} + \frac{\sin(m \arccos(x))m}{(1-x^2)^{3/2}}, \quad (3.15)$$

$$T''''_m(x) = \frac{\cos(m \arccos(x))m^4}{(1-x^2)^2} - 6\frac{\sin(m \arccos(x))m^3x}{(1-x^2)^{5/2}} - 15\frac{\cos(m \arccos(x))m^2x^2}{(1-x^2)^3} - 4\frac{\cos(m \arccos(x))m^2}{(1-x^2)^2} + 15\frac{\sin(m \arccos(x))mx^3}{(1-x^2)^{7/2}} + 9\frac{\sin(m \arccos(x))mx}{(1-x^2)^{5/2}}. \quad (3.16)$$

For $x = \pm 1$, one obtains after a series expansion around $x = \pm 1$

$$T'_m(\pm 1) = (\pm 1)^{m+1}m^2, \quad (3.17)$$

$$T''_m(\pm 1) = \frac{1}{3}(\pm 1)^m m^2(m^2 - 1), \quad (3.18)$$

$$T'''_m(\pm 1) = \frac{1}{15}(\pm 1)^{m+1} m^2(m^2 - 1)(m^2 - 2), \quad (3.19)$$

$$T''''_m(\pm 1) = \frac{1}{105}(\pm 1)^m m^2(m^2 - 1)(m^2 - 2)(m^2 - 3). \quad (3.20)$$

3.2 Numerical implementation

For the temporal stability analysis, it is assumed that the wave number α , Reynolds number Re , density ratio r , viscosity ratio m and Weber number

We (all real) are given. The eigenvalue problem consists of finding complex wave speeds c for which the linear stability problem has non-trivial solutions. The first step towards the solution is to substitute the equation resulting from the continuity of velocity in x -direction (2.44) into the equation resulting from the continuity of normal stress (2.61), which renders the resulting equation linear in c .

The coefficients in the equations for the exact solution for the part of the domain above the virtual interface depend on the yet unknown eigenvalue c nonlinearly ($\gamma = \gamma(\alpha, c, Re)$). These equations are not linearized, but after assuming a value for c , the resulting eigenvalue problem is solved and the (new) value of c is used to obtain a better approximation for the eigenvalue. The numerical calculations show that there is no real need to iterate, i.e., the solution away from the virtual interface does not depend strongly on the value of c chosen in the exact solution for the region above the virtual interface. All these computations use as an initial guess of c equal to zero. This simplification results in a set of equations which is linear in the complex wave speed c .

The Chebyshev polynomials are defined on the interval $[-1, 1]$, therefore the Orr-Sommerfeld equations in the upper and lower fluid are transformed to this interval. For the upper fluid, the transformation

$$z_1 = -\frac{2y}{y_i} + 1 \quad (3.21)$$

is used and for the lower fluid the transformation

$$z_2 = -\frac{2y}{y_w} + 1 \quad (3.22)$$

is used. For both layers, the interface at $y = 0$ is denoted by $z_1 = 1$ and $z_2 = 1$, respectively.

Assume that both $\phi(z_1)$ and $\chi(z_2)$ can be approximated by a truncated series of Chebyshev polynomials, i.e.,

$$\phi(z_1) \approx \sum_{m=0}^{IM} a_m T_m(z_1), \quad (3.23)$$

$$\chi(z_2) \approx \sum_{m=0}^{IN} b_m T_m(z_2), \quad (3.24)$$

where the first $IM + 1$ polynomials are used to approximate $\phi(z_1)$ and the first $IN + 1$ polynomials for $\chi(z_2)$ adding up to a total of $IM + IN + 2$ unknown

coefficients, a_m , $m = 0(1)IM$ and b_m , $m = 0(1)IN$. Upon substitution of above approximations in the Orr-Sommerfeld equations for both fluid layers, the equations are imposed at a finite number of collocation points in the upper and lower layer. As collocation points for the upper layer a variation of the $IM - 3$ Gauss-Lobatto points are chosen, i.e.,

$$z_1 = \cos \frac{\pi(j-1)}{IM-2}, \quad j = 2(1)IM - 2, \quad (3.25)$$

while for the lower fluid layer similar $IN - 3$ points are chosen, i.e.,

$$z_2 = \cos \frac{\pi(j-1)}{IN-2}, \quad j = 2(1)IN - 2. \quad (3.26)$$

These points are the maximums of the $(IM-2)$ -th and $(IN-2)$ -th Chebyshev polynomial, respectively. This collocation method results in $IM-3+IN-3 = IM + IN - 6$ discrete equations. The boundary conditions at the wall give rise to 2 equations, the interface conditions and the virtual interface conditions add another $4+4 = 8$ conditions. Totally, $IM+IN+4$ equations are obtained for the same number of unknowns ($IM+1$ a_n 's, $IN+1$ b_n 's, D and E).

The resulting homogeneous system of linear equations for the unknown coefficients constitutes a generalized eigenvalue problem, $\mathbf{A}\vec{x} = c\mathbf{B}\vec{x}$, where \mathbf{A} and \mathbf{B} are matrices and \vec{x} , the eigenfunction is the column vector containing the unknown coefficients of the Chebyshev polynomials and the two of the exact solution in the region beyond $y = y_i$ and c is the eigenvalue (complex wave speed).

The presence of rows filled with zeros in matrix \mathbf{B} introduces infinite eigenvalues. These spurious eigenvalues will be removed to improve the accuracy of the other eigenvalues. Say row k of \mathbf{B} is filled with only zeros. Linear column operations (Gaussian elimination) are performed to fill row k in \mathbf{A} also with zeros except for the element in column l . Mathematically stated, element (i,j) of \mathbf{A} and \mathbf{B} are modified (indicated by a star) to give (except for $j = l$)

$$\mathbf{A}^*(i, j) = \mathbf{A}(i, j) - \mathbf{A}(i, l) \frac{\mathbf{A}(k, j)}{\mathbf{A}(k, l)} \quad (3.27)$$

$$\mathbf{B}^*(i, j) = \mathbf{B}(i, j) - \mathbf{B}(i, l) \frac{\mathbf{A}(k, j)}{\mathbf{A}(k, l)}. \quad (3.28)$$

Row k now holds the equation that x_l is equal to zero. The infinite eigenvalue can be removed by deleting column l and row k without changing any of the

finite eigenvalues. Above process is repeated until \mathbf{B} does not contain rows filled with only zeroes.

Instead of removing the infinite eigenvalues, one can also multiply the equations which do not involve \mathbf{B} with c , thereby changing the infinite eigenvalue to zero. Numerical computations showed that the accuracy of the computed eigenvalues in case of explicitly removing infinite eigenvalues exceeds that of the case of introducing zero eigenvalues. Furthermore, in the latter case the zero eigenvalues are not exactly zero, but in some cases of the same order of magnitude as the largest eigenvalue. This occurred especially for the interfacial mode in two-layer computations. In the following, the infinite eigenvalues are removed explicitly.

After balancing both \mathbf{A} and \mathbf{B} , a QZ-algorithm is used to calculate all the eigenvalues of the resulting system. These eigenvalues are arranged in the order of decreasing magnitude of their imaginary part. Unfortunately, the QZ-algorithm finds a lot of so-called spurious eigenvalues, which have to be removed. Among these spurious eigenvalues, some are easy to trace, as they have a real part of the complex wave speed less than the minimum primary velocity (found at the wall) or greater than the free stream velocity or fall outside Gerschgorin's discs [39]. Others are harder to trace. One spurious eigenvalue was discovered by changing the location of the virtual interface causing the eigenvalue to change substantially indicating that the virtual interface introduced this spurious eigenvalue.

The eigenfunctions are computed after setting $\mathbf{C} = \mathbf{A} - c\mathbf{B}$, where c has been set equal to the eigenvalue with the largest imaginary part. The eigenfunction is found by searching a non-trivial solution of $\mathbf{C}\mathbf{x} = 0$. Such a non-trivial solution exists since the determinant of \mathbf{C} is identical to zero. One of the unknown coefficients (a_1) is set equal to unity, an arbitrary equation (row) is removed and the corresponding set of linear equations ($\mathbf{D}\vec{x} = \vec{e}$) can be solved using an LU-decomposition algorithm.

Hereafter, it is straightforward to compute the stream function in both layers using equations (3.23) and (3.24). The distribution of the velocity components follow from equations (2.22) and (2.23) and the pressure disturbances from (2.25) and (2.27). In all plots of these distributions in the following chapters, the x - and t -dependency, i.e. $e^{i\alpha(x-ct)}$ has been disregarded, i.e., only the amplitude of the wave-like solutions is plotted. When calculating the energy and enstrophy distribution, one has to take the real part of the complex quan-

tities like velocity and pressure, because the corresponding expressions are not linear in these quantities.

Chapter 4

One-layer flow

4.1 One-layer Blasius flow

The theory of the previous two chapters will, as a first example, be applied to the similarity Blasius boundary-layer profile. Instead of a lower fluid layer, a fixed wall will be assumed at $y = 0$. The equation governing the linear temporal stability is given by (2.30) and the boundary conditions are the no-slip conditions at the solid wall and the four conditions at the virtual interface to match the perturbed Blasius solution with the analytical perturbed free-stream solution. The primary velocity profile is given in figure 2.3 for $y > 0$. The one-layer Blasius flow will be used to check the results with results from the literature and to compare in the next chapter with results for two-layer flows.

4.1.1 Numerical parameters

First, the effect of the number of Chebyshev polynomials used and the influence of the location of the virtual interface, two non physical parameters in the model, will be discussed. Figure 4.1 gives the imaginary part of the complex wave speed c_i as a function of the wave number α for several number of Chebyshev polynomials. The Reynolds number is set at 1000, which can be reached by assuming, for example, $x^* = 0.5m$, $U_\infty^* = 30 \frac{m}{s}$ and using the kinematic viscosity of air at 278K, $\nu^* = 1.40 \times 10^{-5} \frac{m^2}{s}$. This results in a

boundary-layer thickness of about $3mm$ and a boundary-layer displacement thickness of $0.8mm$. The wave numbers plotted correspond with wave lengths between $0.8cm$ and $6cm$. The values used are in good agreement with the experimental observed waves and Reynolds number. The virtual interface is set well outside the boundary-layer at $y_i = 10$.

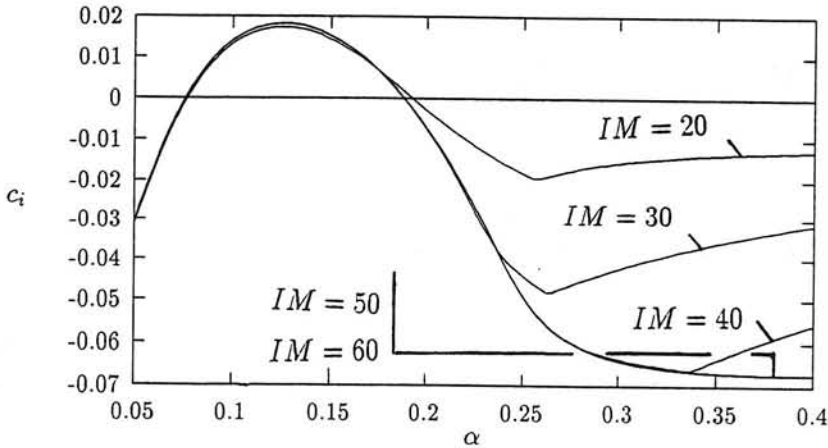


FIGURE 4.1: Growth factor for Blasius flow ($y_i = 10, Re = 1000$), ($c_i > 0$: unstable flow)

Figure 4.1 shows that the solution is converged for about 50 Chebyshev polynomials. For fewer Chebyshev polynomials, the solution is converged only for small wave numbers. The region of instability, the most interesting part, is already computed accurately with 30 Chebyshev polynomials.

The kink in the computed curves for a low number of Chebyshev polynomials is the result of a different (spurious) mode becoming the least stable one. This can be determined by looking at the real part of the complex wave speed c_r , which is discontinuous at the kink in c_i , in the present case jumping from a value below 0.5 to one above 0.75.

The spectral method obtains exponential accuracy which is depicted in figure 4.2. For a wave number of 0.20 and a Reynolds number of 1000, the relative error is plotted as a function of IM . As a result most of the following computations will use 61 ($IM + 1$) Chebyshev polynomials (in the upper layer) to compute the numerical solution.

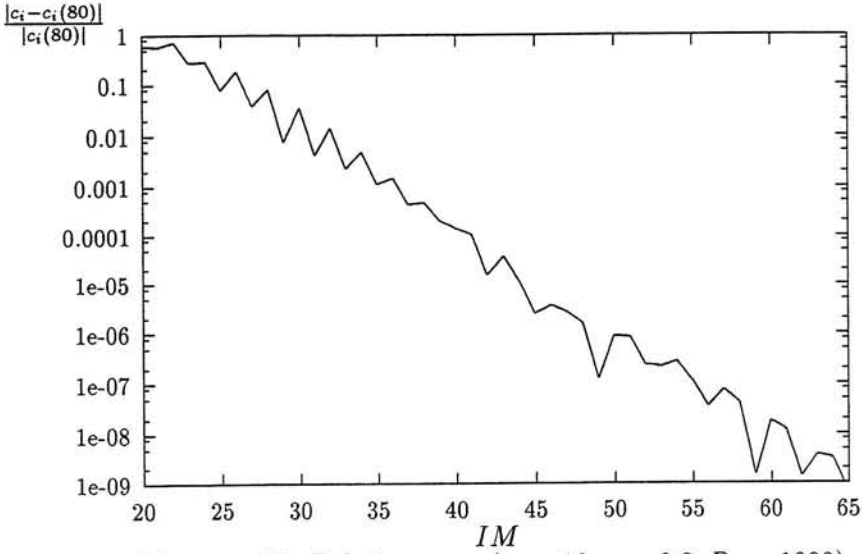


FIGURE 4.2: Relative error ($y_i = 10, \alpha = 0.2, Re = 1000$)

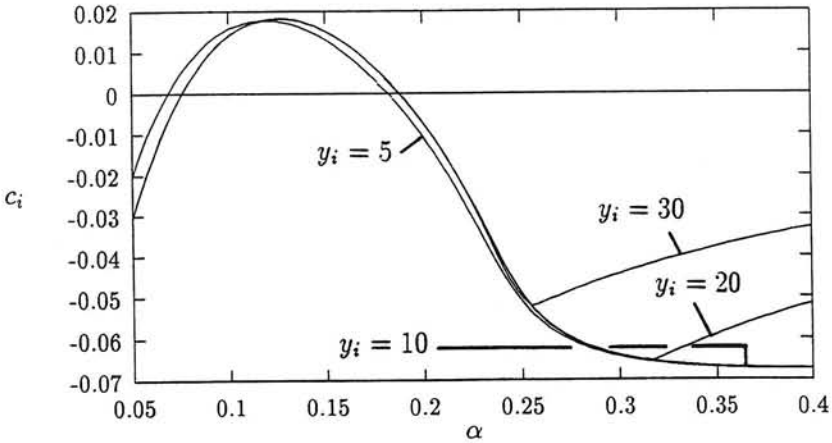


FIGURE 4.3: Growth factor for Blasius flow ($IM = 60, Re = 1000$)

The influence of the location of the virtual interface is plotted in figure 4.3 for interface locations $y_i = 5, 10, 20$ and 30 . Again IM is set equal to 60 and a Reynolds number of 1000 is used. Note that by increasing y_i the density of the collocation points diminishes. For $y_i = 5$, still inside the boundary-layer, the stability curve is not computed accurately. For locations of the virtual interface above 10 , the stability curves coincide except for large wave numbers. However, by increasing the number of Chebyshev polynomials used for the computations of the virtual interface at $y_i = 20$ and $y_i = 30$ the stability curves are identical to the one for $y_i = 10$. From here on, the location of the virtual interface is set equal to $y_i = 10$.

4.1.2 Stability curves

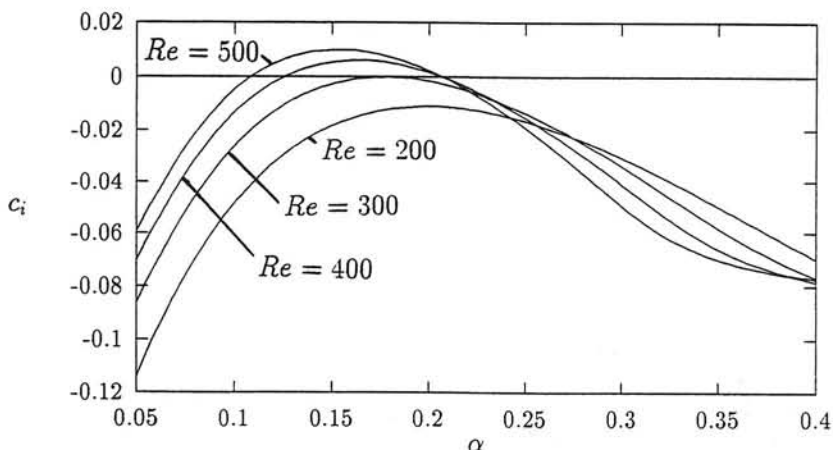


FIGURE 4.4: Growth factor for Blasius flow ($y_i = 10, IM = 60$)

Figure 4.4 gives the maximum imaginary part of the complex wave speed (c_i) for several Reynolds numbers. As stated before, the virtual interface is located at $y_i = 10$ and 61 Chebyshev polynomials are used to compute the solution. It is seen that for small Reynolds numbers the flow is stable for all wave numbers plotted. By increasing the Reynolds number, the flow will become unstable at Re just above 300 , which is in good agreement with the value found in the literature. By further increasing the Reynolds number the region of instability will grow and shift towards smaller wave numbers or equivalently larger wave lengths. The corresponding wave speeds (c_r) are presented in figure 4.5.

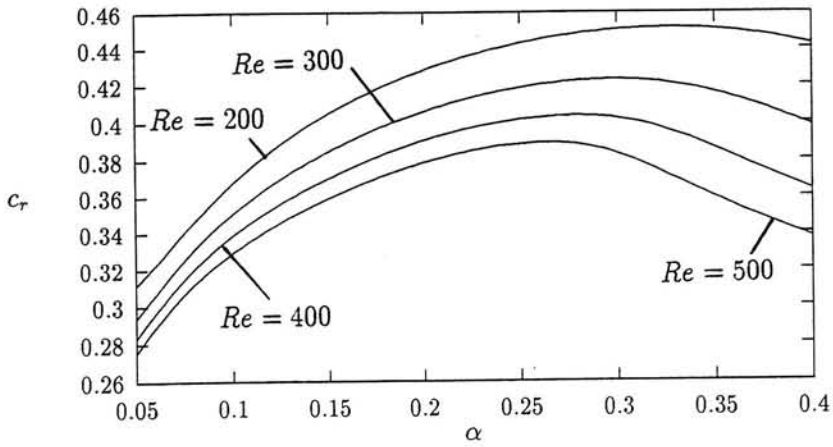


FIGURE 4.5: Wave speed for Blasius flow ($y_i = 10, IM = 60$)

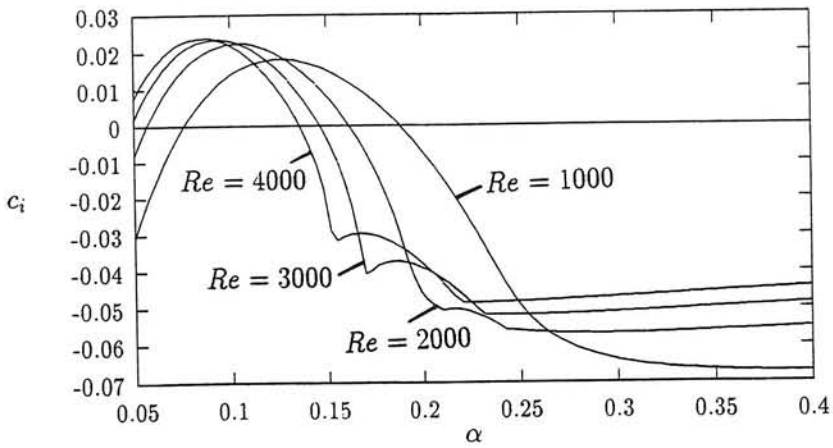


FIGURE 4.6: Growth factor for Blasius flow ($y_i = 10, IM = 60$)

It is seen that by increasing the Reynolds number the wave speed becomes smaller at each wave number. Furthermore, the most unstable waves exhibit wave speeds between 25% and 45% of the undisturbed free stream speed. This corresponds to y -locations between 1 and 2 in the basic velocity profile.

The stability curves for Reynolds numbers above 1000 are given in figure 4.6. It is interesting to note that the wave number at which the flow turns unstable becomes smaller as the Reynolds number increases, while also the region of instability shifts to lower values of the wave number region and becomes smaller. For Reynolds number above 2000, a hump is visible in the neighbourhood of $\alpha = 0.2$. This hump corresponds to a different mode of (in)stability becoming dominant, as can be seen in figure 4.7 giving the wave speed as a function of the wave number.

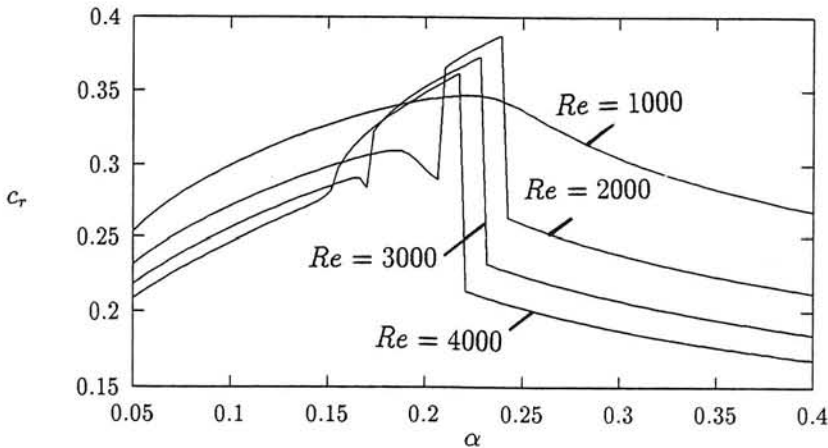


FIGURE 4.7: Wave speed for Blasius flow ($y_i = 10, IM = 60$)

At the location of the hump, there is a discontinuity in the wave speed indicating that the least stable mode is a different one having a wave speed greater than the other mode, but still smaller than 50% of the free stream velocity. Clearly, by increasing the Reynolds number the wave speed becomes smaller. The critical point, defined as the location where the wave speed is equal to the basic velocity, moves in the direction of the solid wall with increasing Reynolds number.

4.1.3 Perturbation quantities

Figure 4.8 gives the magnitude of the complex eigenfunction $\phi(y)$ throughout the layer for two different wave numbers. The Reynolds number is set equal to 1000. The number of Chebyshev polynomials used is 101. This is a higher number than the 61 used standard to compute the eigenvalues, but calculations show that an accurate determination of the eigenfunction and its derivatives requires about 100 polynomials.

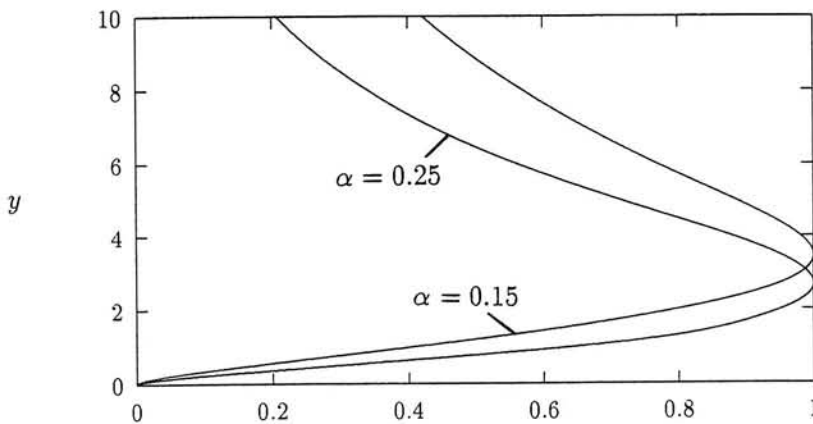


FIGURE 4.8: Magnitude of the eigenfunction ($y_i = 10$, $IM = 100$, $Re = 1000$)

In all these computations, the stream function $\tilde{\Phi}$ is normalized such that its largest magnitude is equal to unity while its phase angle at that location is set equal to zero. The perturbations in the velocity components in x - and y -direction just as the pressure disturbance follow easily from the stream function using the expressions given in chapter 2.

The wave numbers chosen, $\alpha = 0.15$ and $\alpha = 0.25$ correspond to an unstable ($\alpha = 0.15$) and a stable ($\alpha = 0.25$) condition. As required the eigenfunction is equal to zero at the wall. The maximum value of the eigenfunction is obtained at a lower y -location for the stable mode than for the unstable mode. For the stable mode, the gradients are also steeper. Above the virtual interface, the eigenfunction will decay exponentially as indicated by the exact solution of the stability problem.

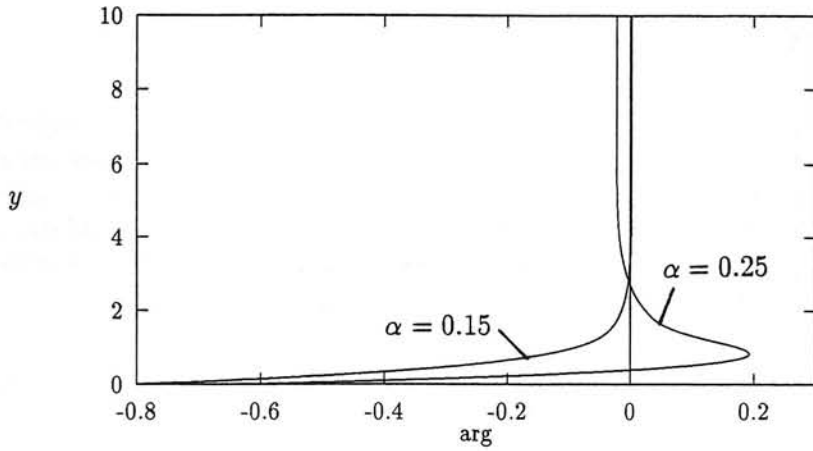


FIGURE 4.9: Phase angle eigenfunction ($y_i = 10, IM = 100, Re = 1000$)

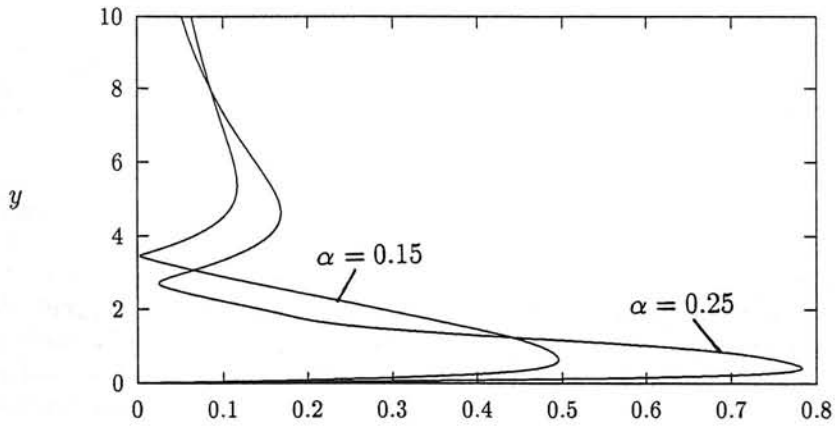


FIGURE 4.10: Magnitude of the x -component velocity perturbation ($y_i = 10, IM = 100, Re = 1000$)

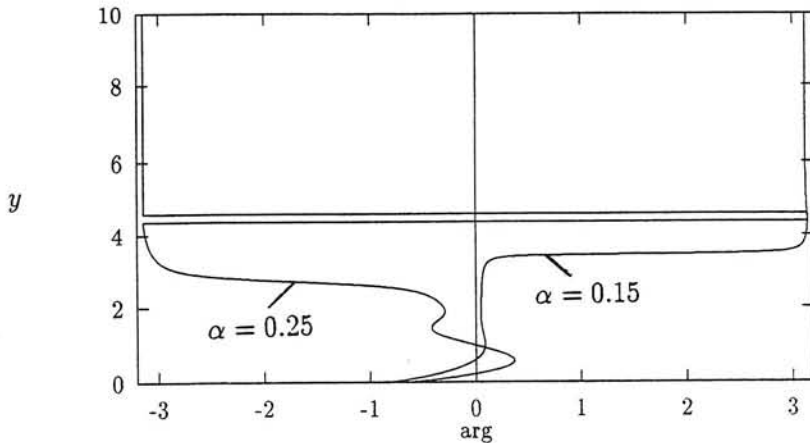


FIGURE 4.11: Phase angle x -component velocity perturbation ($y_i = 10, IM = 100, Re = 1000$)

The phase angle of the eigenfunction is given in figure 4.9. Note that the phase angle is chosen equal to zero at the maximum value of the eigenfunction. At the wall, both for the stable and the unstable wave number, the phase angle of the eigenfunction is lagging the phase angle of the maximum value of the eigenfunction. The phase angle of the unstable wave number is a monotonically increasing function of the distance from the wall contrary to the phase angle of the stable wave number, which changes sign.

The next two figures (4.10 and 4.11) give the magnitude of the velocity perturbation in x -direction and the phase angle of this velocity. It is interesting to note that there are the two maximums in the velocity perturbations and the location where there is nearly no perturbation at both wave numbers (a knot). The phase angle of the velocity perturbation in x -direction tends to π when moving away from the wall.

The velocity perturbation in the y -direction is given in figure 4.12. one notices that the perturbations in y -direction are smaller than the one in x -direction by about a factor 0.5. There is also only one maximum in the velocity profile.

Figure 4.13 shows that the velocity perturbation in the y -direction is $\pi/2$ out of phase with the velocity perturbation in the x -direction in the far field. This indicates that when one of the velocity components reaches its maximum (or

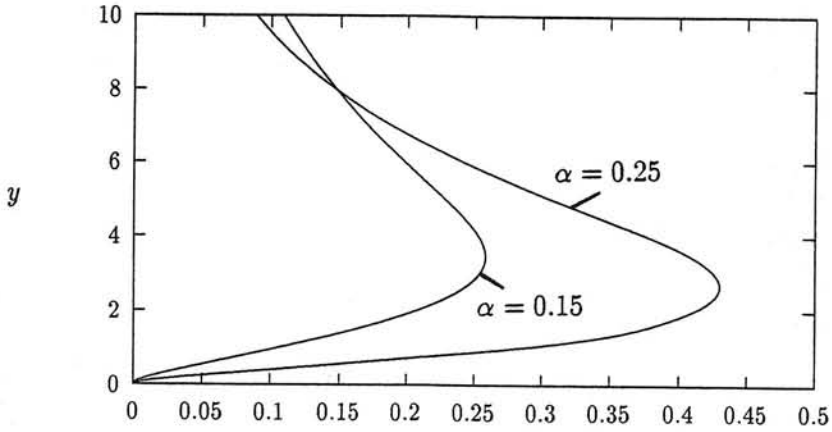


FIGURE 4.12: Magnitude of the y -component velocity perturbation ($y_i = 10, IM = 100, Re = 1000$)

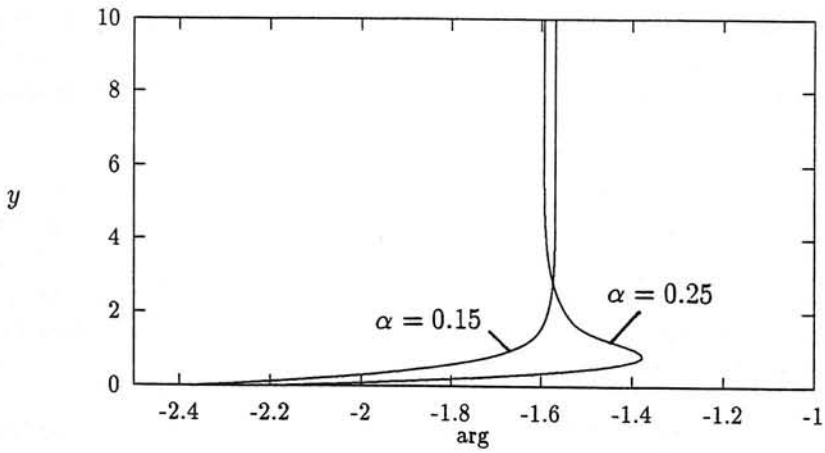


FIGURE 4.13: Phase angle y -component velocity perturbation ($y_i = 10, IM = 100, Re = 1000$)

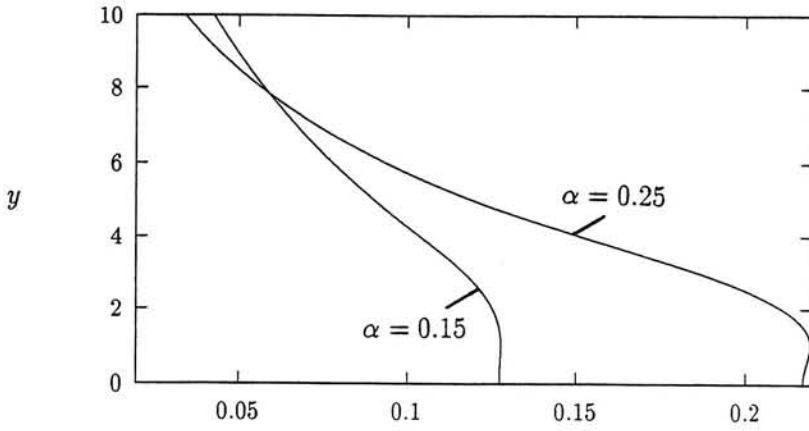


FIGURE 4.14: Magnitude of the pressure perturbation ($y_i = 10, IM = 100, Re = 1000$)

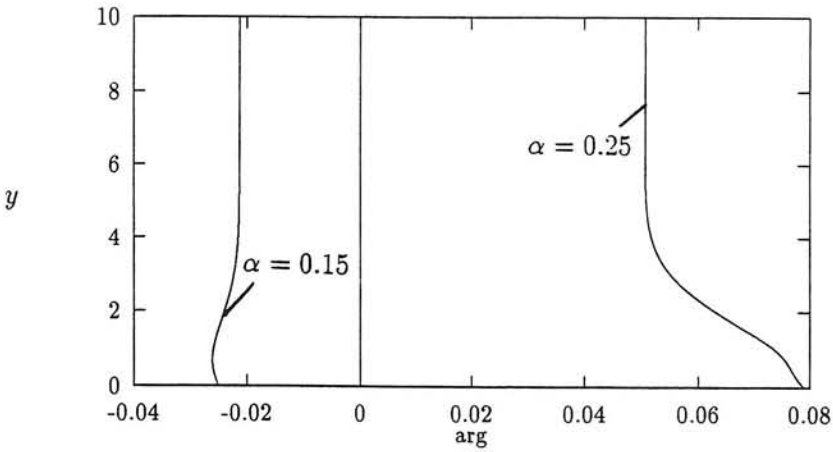


FIGURE 4.15: Phase angle pressure perturbation ($y_i = 10, IM = 100, Re = 1000$)

minimum) the other one passes through zero.

The distribution of the pressure perturbation is given in figure 4.14. Both curves have a maximum just next to the wall. The pressure disturbance of the stable flow obtains a larger value, and decays more rapidly to zero than the curve corresponding to the unstable wave number.

The phase angle of the pressure disturbance does not vary much as indicated in figure 4.15. The pressure disturbances are $\pi/2$ out of phase with the velocity perturbation in the y -direction and π out of phase with the velocity perturbation in the x -direction.

4.1.4 Energy considerations

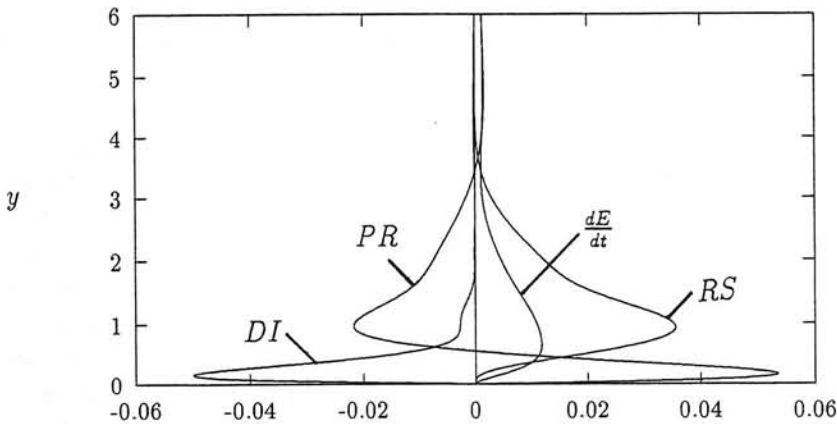


FIGURE 4.16: Mechanical energy balance ($y_i = 10, IM = 100, Re = 1000, \alpha = 0.15$)

The mechanical energy balance is depicted in figure 4.16 for an unstable wave number ($\alpha = 0.15$) and a Reynolds number equal to 1000. The instability is indicated by the positive sign of $\frac{dE}{dt}$ throughout the layer. It is easy to prove that if $\frac{dE}{dt}$ is greater than zero (or less than zero) at one position, it is greater than zero throughout the layer (or less than) using the definition of $\frac{dE}{dt}$. Near the wall, the instability is driven by the interaction of the pressure disturbance and the velocity disturbances, while further away from the wall, the Reynolds

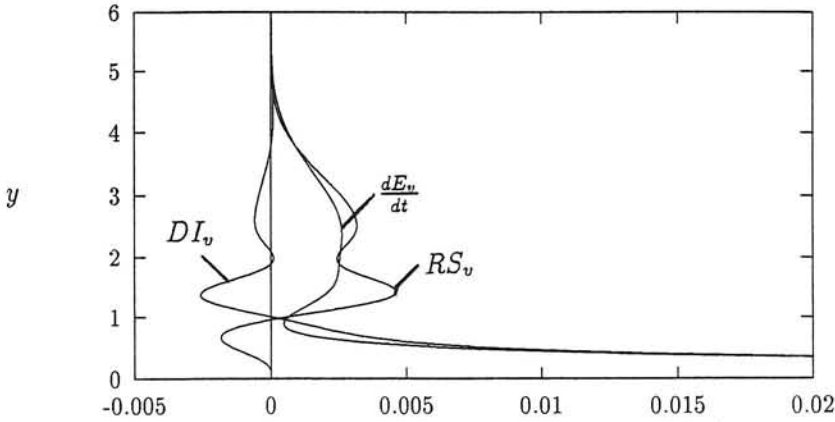


FIGURE 4.17: Entrophy balance ($y_i = 10, IM = 100, Re = 1000, \alpha = 0.15$)

stress term causes the instability. On the other hand, near the wall, the dissipation term counteracts the growth of the instability as the pressure term does further away from the wall. This energy distribution is typically for the Blasius instability.

The change in entrophy with respect to time is given in figure 4.17 for the unstable wave number. A very sharp peak near the solid wall is the characteristic feature of this picture. This feature is one of the main reasons for the high number of Chebyshev polynomials needed to compute the distribution accurately. The entrophy increases with time throughout the fluid layer. Near the wall the effects of the viscous forces produce the accumulation and further away from the wall, the interaction of the basic flow and the velocity perturbations are the main cause of instability. It is interesting to note that the viscous forces destabilize the entrophy and on the other hand stabilize the kinetic energy. However if the kinetic energy accumulates in time, so will the entrophy.

The mechanical energy distribution for a stable wave number ($\alpha = 0.25$) is plotted in figure 4.18. The change of kinetic energy with respect to time is negative throughout the fluid layer. Near the wall, the effects of viscosity stabilize the fluid flow. Further away from the wall, the pressure term is the most dominant stabilizing factor. Even further away, the Reynolds stress stabilizes the flow and in the far field the pressure term is stabilizing again.

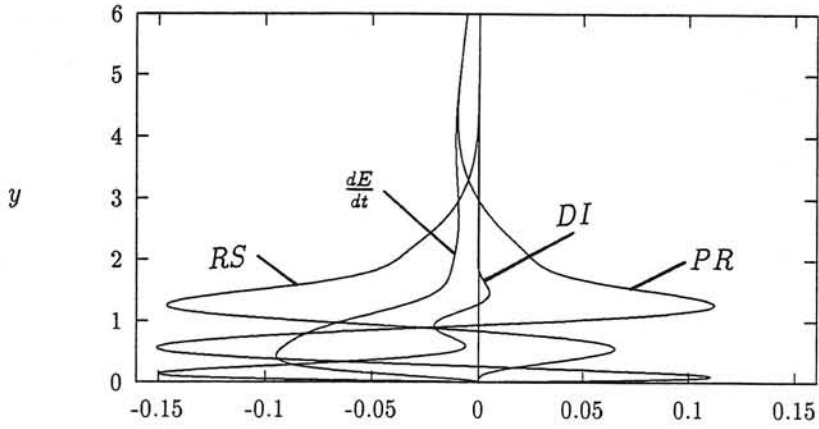


FIGURE 4.18: Mechanical energy balance ($y_i = 10, IM = 100, Re = 1000, \alpha = 0.25$)

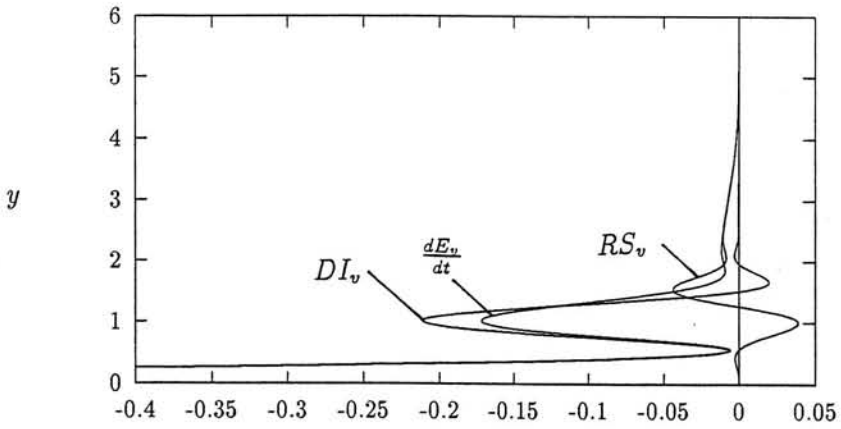


FIGURE 4.19: Enstrophy balance ($y_i = 10, IM = 100, Re = 1000, \alpha = 0.25$)

Figure 4.19 gives the origin of the change in enstrophy throughout the fluid layer. Again a very distinct peak near the solid wall, where the effects of viscosity reduce the amount of enstrophy in time.

After integrating the energy distribution not only over one wave length, but also over the fluid layer (actually to infinity, numerically only to the virtual interface, assuming that the perturbations above the virtual interface are negligible), one gets figure 4.20 for a Reynolds number of 1000. The uniformly distributed points (in total NO_P) in the y -direction (here: 2000) at which location the eigenfunction is computed (the points of the mid-point quadrature) is fairly high. However, computations have revealed that if one integrates throughout the layer in y -direction, this accuracy is needed in order to resolve all aspects of the solution sufficiently, especially near the solid wall and near the virtual interface.

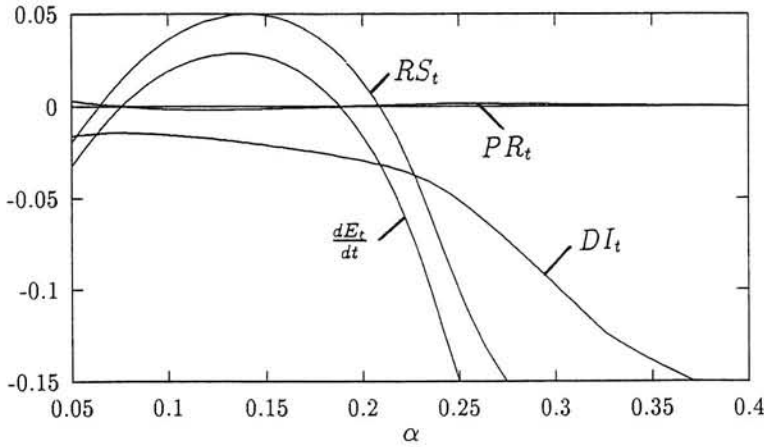


FIGURE 4.20: Mechanical energy balance ($y_i = 10, IM = 100, NO_P = 2000, Re = 1000$)

The region of instability is indicated where $\frac{dE}{dt}$ is greater than zero. This region corresponds to the one given in figure 4.6. Clearly the overall instability is driven by the Reynolds stress. It can be shown that the pressure term integrates to zero analytically. This result only holds in the case of a one-layer flow bounded by a solid wall. The discrepancy between the curve PR and zero is due to the virtual interface at $y_i = 10$, where the quadrature has been stopped. The dissipation is always less than zero, as can be proven analytically in the case of a one-layer flow bounded by a fixed wall.

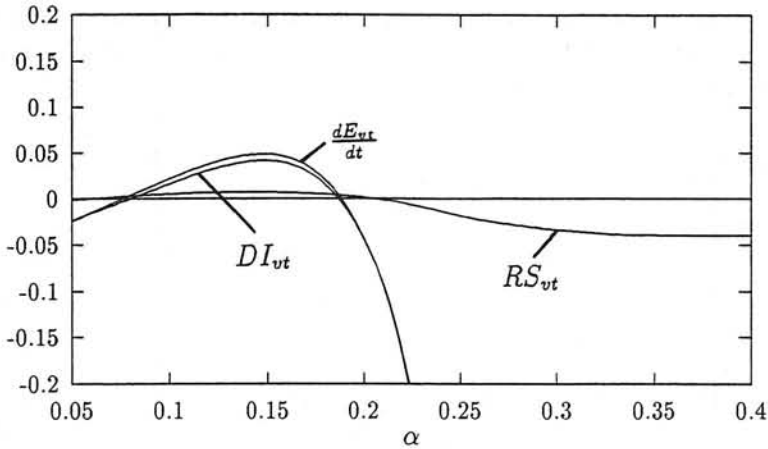


FIGURE 4.21: Enstrophy balance ($y_i = 10, IM = 100, NOP = 2000, Re = 1000$)

The origin of the change in enstrophy is given in figure 4.21 for a Reynolds number of 1000 and several wave numbers. The region of instability corresponds to the one given in the previous figure. The growth of the enstrophy is caused by the viscous forces. The influence of the Reynolds stress on the rate of change of enstrophy is negligible regarded with respect to the viscous forces.

4.2 Calculations without the virtual interface

Instead of using a virtual interface, one can also map the region from zero to infinity onto $[-1,1]$ before substitution of the Chebyshev polynomials. Calculations have been performed using an algebraic transformation given by $z = \frac{1-\frac{y}{a}}{1+\frac{y}{a}}$, where a is a constant used to change the distribution of the grid points. By increasing a , the collocation points are more spread out in the boundary-layer. Next to this algebraic transformation, the exponential transformation $z = 1 - 2 \tanh \frac{y}{a}$ has been used, where the parameter a has the same effect as for the algebraic transformation.

At infinity, the boundary condition that the first derivative with respect to y

of the stream function has to equal zero is automatically satisfied. Therefore, at infinity, $\frac{dz}{dy}$ will be required to be equal to zero. To reduce numerical and computational errors, the second derivative, $\frac{d^2z}{dy^2}$ is also set equal to zero. To obtain the same number of unknowns as equations, as collocation points in the upper layer $z = \cos \frac{\pi(j-1)}{IM-3}$ will be used where $j = 2(1)IM - 3$, i.e., the collocation points correspond to the maximums of the $IM - 3$ -th Chebyshev polynomial.

The numerical results obtained without the virtual interface are in good agreement with the results obtained with the virtual interface. However, some differences should be emphasized here. First, the calculations without the virtual interface do not require the iteration needed in the analytical solution. In the case of a virtual interface, every mode should be computed separately, because above the virtual interface only one complex wave speed can be evaluated at a time. Without the virtual interface, all modes can be computed at the same time. However, the most unstable mode is the most interesting one. The calculations without the virtual interface require more collocation points to obtain the same accuracy as in the case with the virtual interface.

Furthermore, the dependency on the wave number of the number of collocation points needed for good accuracy is very large. For accurate results of a wave number of about 0.2, one needs about 100 polynomials in the gas layer at least. For smaller wave numbers, this number increases rapidly to over 200 polynomials for $\alpha = 0.1$, thereby also increasing the computational costs. The computational costs scale with the total number of Chebyshev polynomials in both layers cubed. For these reasons, all the two-layer computations have been performed using the virtual interface.

Chapter 5

Two-layer flow

5.1 Air stream over anti-icing fluid

5.1.1 Stability curves

This section discusses the results of the stability analysis for two-layer flows. As an example the air flow over a thin layer of anti-icing is chosen. The physical data of the anti-icing fluid is obtained from the Von Kármán Institute in Belgium [29]. The non-dimensional depth of the liquid layer is set equal to $y = 1$. Recall that the boundary-layer ends at about $y = 6$. Note, that the dimensional depth increases if one moves further away from the beginning of the Blasius boundary-layer profile. The liquid layer is assumed to be non-Newtonian with a power-law coefficient equal to $n = 0.82$. The density ratio r is set equal to 1400 and the ratio $\frac{k_2}{\mu_1}$ is equal to 56000, which makes $m = 1.07 \times 10^4$ upon assuming that $\frac{U_\infty^*}{L^*} = 10000$, which corresponds for example with a undisturbed velocity of $30 \frac{m}{s}$ and a thickness of the lower layer of $3mm$.

The virtual interface is positioned at $y_i = 10$. Several computations have been performed with different number of Chebyshev polynomials in each layer. The results showed that the eigenvalues are computed accurately for about 40 polynomials in each layer. Here 61 polynomials are used in both the upper and the lower fluid layer. If one wants to compute the energy and especially the enstrophy distribution, 61 polynomials are not sufficient. 101 polynomials in each layer will facilitate an accurate representation.

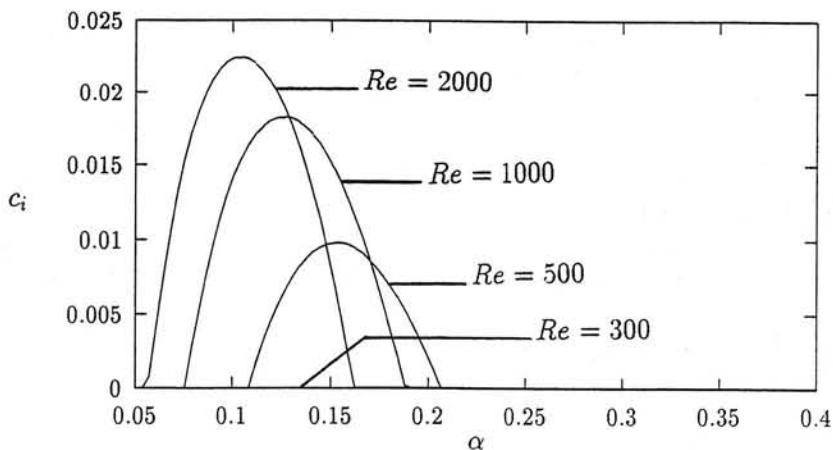


FIGURE 5.1: Growth factor two-layer flow ($y_i = 10, IM = IN = 60, m = 1.07 \times 10^4, n = 0.82, r = 1400, y_w = -1$)

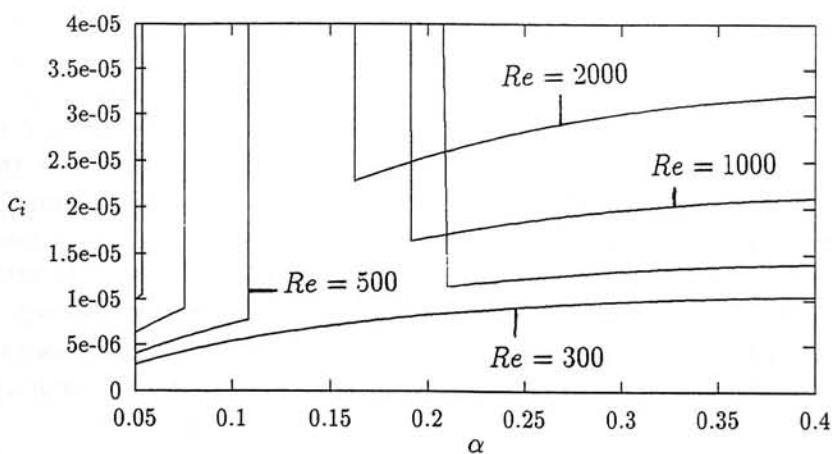


FIGURE 5.2: Growth factor two-layer flow ($y_i = 10, IM = IN = 60, m = 1.07 \times 10^4, n = 0.82, r = 1400, y_w = -1$)

In figure 5.1 the stability curves for Reynolds numbers of 300, 500, 1000 and 2000 are depicted for wave numbers between 0.05 and 0.4. The curve for a Reynolds number of 300 lies just above the x -axis and is not visible in figure 5.1. Three distinct humps for $Re = 500, 1000$ and 2000 are very clearly visible. These humps correspond accurately with the humps plotted in figure 4.4 and 4.6 for Blasius flow solely. This instability is therefore caused by the presence of the air stream and referred to as the Blasius mode. However, next to this Blasius mode, another mode of instability appears due to the presence of the fluid layer.

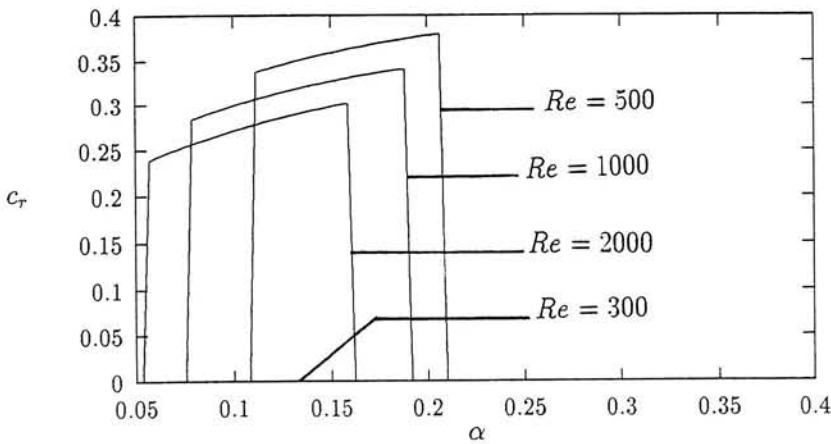


FIGURE 5.3: Wave speed for two-layer flow ($y_i = 10, IM = IN = 60, m = 1.07 \times 10^4, n = 0.82, r = 1400, y_w = -1$)

This mode is called the interfacial mode. For clarity figure 5.1 has been scaled to give figure 5.2. This interfacial mode is present for all wave numbers considered and the growth rate increases by increasing the Reynolds number. However, for very small wave numbers, the flow is stable (not shown).

The wave speed is given in figure 5.3 and enlarged near the x -axis in figure 5.4. The wave speeds of the Blasius mode correspond very well with the speeds found in the one-layer case. The wave speeds of the interfacial mode are close to zero. Remember that for the computations the interfacial velocity is set equal to zero. Therefore, the critical point for the interfacial mode is just above the interface. This also stresses the fact that the interface is the main cause of the instability.

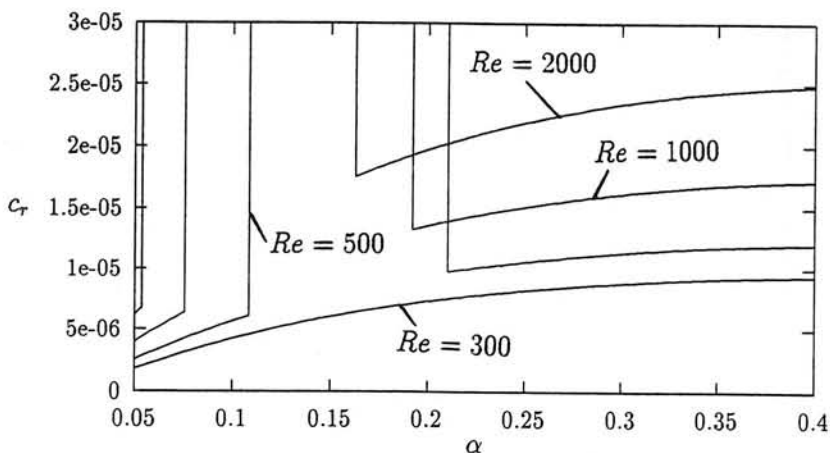


FIGURE 5.4: Wave speed for two-layer flow ($y_i = 10, IM = IN = 60, m = 1.07 \times 10^4, n = 0.82, r = 1400, y_w = -1$)

5.1.2 Perturbation quantities

The eigenfunctions are normalized in the same manner as in the one-layer case, i.e., the maximum magnitude of the stream function ($\tilde{\Phi}$) is equal to one. The magnitude of the velocity perturbations in the x -direction are given in figure 5.5 for a Reynolds number of 1000. The perturbations are given for a wave number equal to 0.15, which has the Blasius mode as the driving instability, and a wave number of 0.25, which has the interfacial mode as the driving instability. The perturbations for the Blasius mode are in good agreement with the ones found in the one-layer case. The perturbations in the liquid layer are very small for both wave numbers compared to the ones in the gas layer. This is due to the large difference in viscosity. The velocity perturbation in x -direction for $\alpha = 0.25$ exhibits a sharp peak at the interface and a rapid drop thereafter.

The phase angle for the velocity perturbations in x -direction is given in figure 5.6 for both wave numbers. The phase angle of the y -component of the perturbation velocity in the liquid layer is about $\frac{\pi}{2}$ out of the phase with the phase angle in the far field. Rapid changes in the phase angle are visible for the interfacial mode.

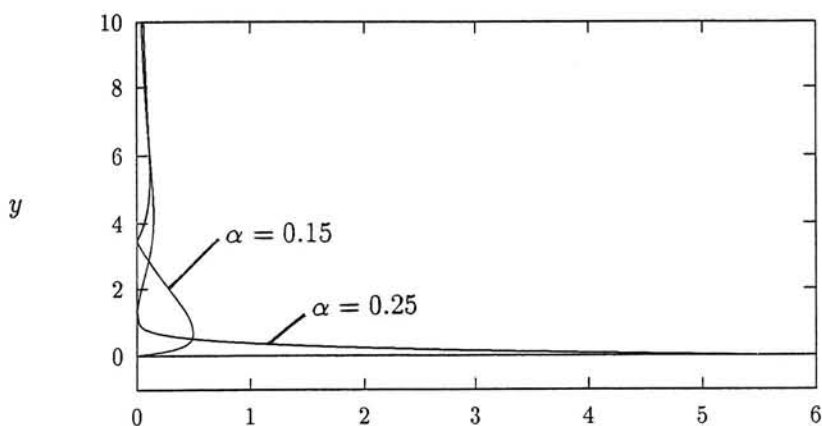


FIGURE 5.5: Magnitude of the x -component velocity perturbation ($y_i = 10, IM = IN = 100, NOP = 2000, m = 1.07 \times 10^4, n = 0.82, r = 1400, Re = 1000, y_w = -1$)

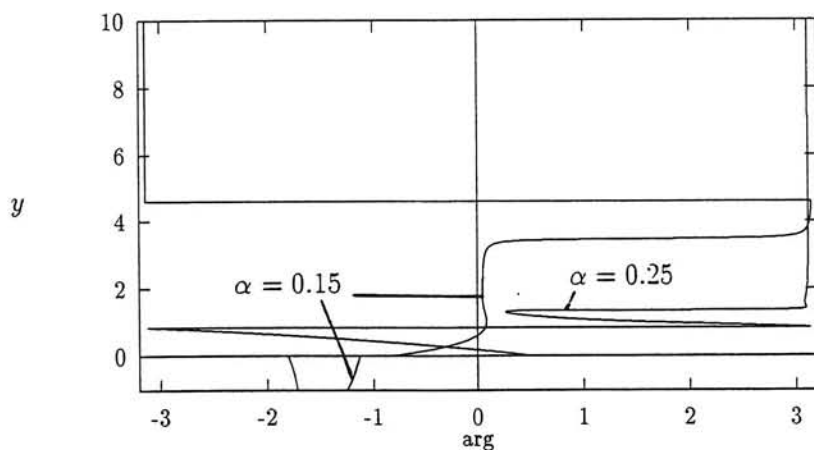


FIGURE 5.6: Phase angle x -component velocity perturbation ($y_i = 10, IM = IN = 100, NOP = 2000, m = 1.07 \times 10^4, n = 0.82, r = 1400, Re = 1000, y_w = -1$)

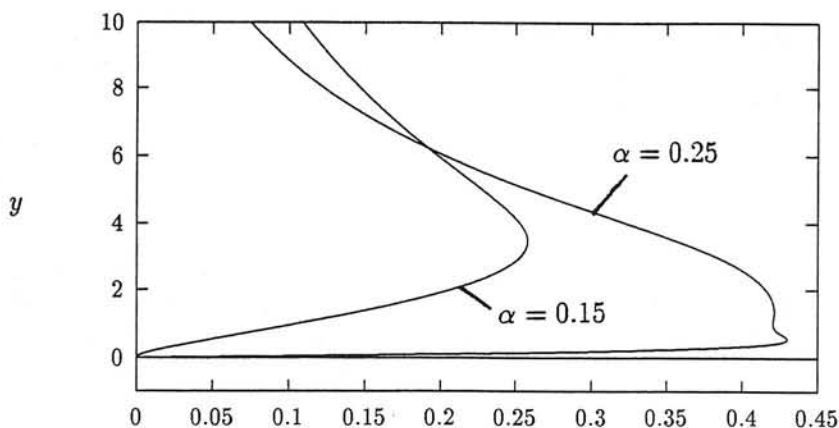


FIGURE 5.7: Magnitude of the y -component velocity perturbation ($y_i = 10, IM = IN = 100, NOP = 2000, m = 1.07 \times 10^4, n = 0.82, r = 1400, Re = 1000, y_w = -1$)

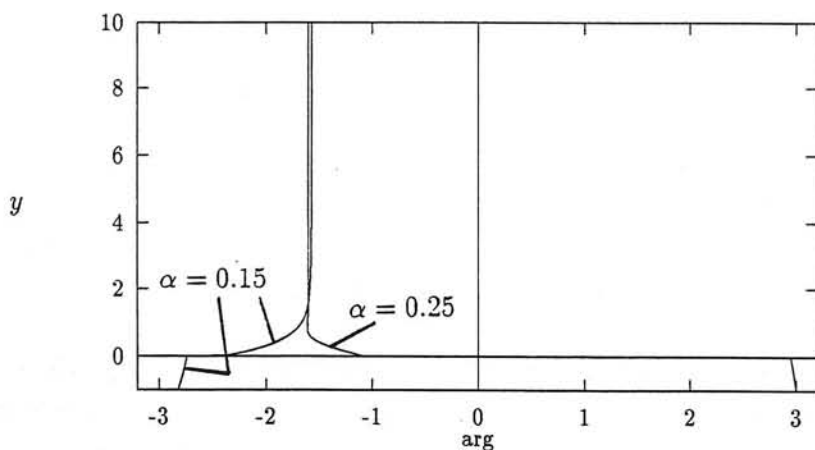


FIGURE 5.8: Phase angle y -component velocity perturbation ($y_i = 10, IM = IN = 100, NOP = 2000, m = 1.07 \times 10^4, n = 0.82, r = 1400, Re = 1000, y_w = -1$)

Figure 5.7 and 5.8 give the magnitude and the phase angle of the velocity perturbations in y -direction for a Reynolds number of 1000 and a wave number of 0.15 and 0.25. Just as for the velocity perturbations in x -direction there are hardly any perturbations in the lower fluid layer. In contrast to the Blasius instability, the interfacial instability has two distinct maximum values in the velocity perturbations.

The plots of the phase angle show that in the lower liquid layer, the velocity perturbations in x - and y -directions are $\frac{\pi}{2}$ out of phase, just as in the upper fluid layer. This phase difference is also established between the liquid layer and the air flow.

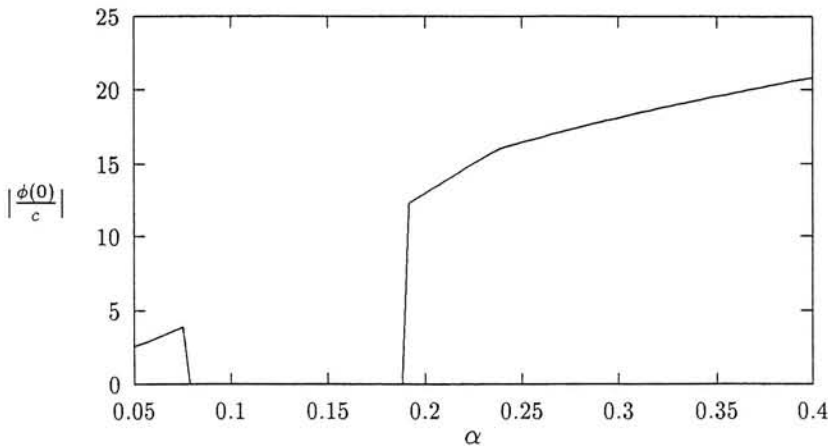


FIGURE 5.9: Magnitude of the interface location ($y_i = 10, IM = IN = 60, m = 1.07 \times 10^4, n = 0.82, Re = 1000, r = 1400, y_w = -1$)

The location of the interface between the fluids is given by (2.40), where it has been assumed that (the magnitude of) $\frac{\phi(0^+)}{c-U_i(0^+)}$ is small (of the same order of magnitude as the other perturbation quantities). This magnitude has been plotted in figure 5.9 for wave numbers from 0.05 to 0.4. The amplitude of the interface displacement for the range in α where the Blasius instability occurs, is fairly small. However, the amplitude of the interface displacement for the interfacial mode is not small. Therefore, precautions have to be taken into account when interpreting the stability results for this mode. Remember, that it has been assumed that the amplitude of the interface is of the same order of magnitude as the velocity and pressure perturbations, which are of order 1.

Several other calculations have been performed using different parameters of m , r and y_w showing that the amplitude of the interface displacement for the interfacial mode is always fairly large.

5.1.3 Energy consideration

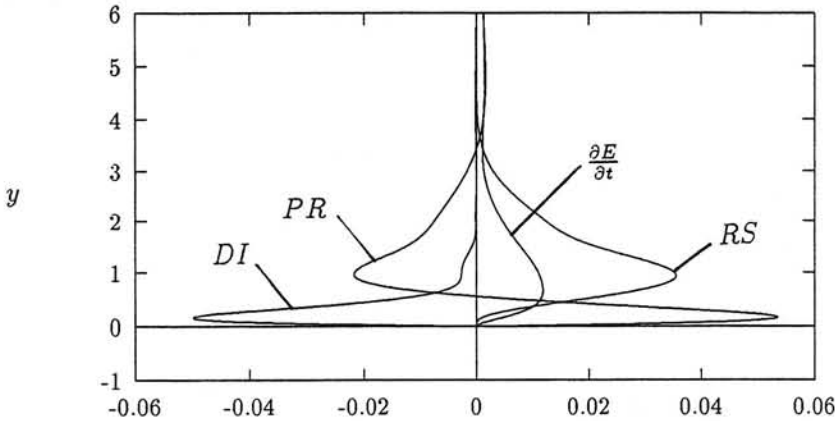


FIGURE 5.10: Mechanical energy balance ($y_i = 10$, $IM = IN = 100$, $NOP = 2000$, $m = 1.07 \times 10^4$, $n = 0.82$, $r = 1400$, $Re = 1000$, $y_w = -1$, $\alpha = 0.15$)

The mechanical energy balance for a Reynolds number of 1000 and a wave number of 0.15 (Blasius mode) is given in figure 5.10. The positive values of the change in kinetic energy throughout the layers indicate the presence of the instability. In the lower layer, the instability is driven by the pressure term (not visible on the scale plotted) and stabilized by the action of dissipation. The Reynolds stress is in this case equal to zero because the second derivative of the primary velocity in the liquid layer equals zero. In the gas layer, the mechanical energy balance is similar to that of the one-layer case. Near the interface, the instability is driven by the pressure term and further away by the Reynolds stress.

The distribution of the enstrophy is given in figure 5.11 for $Re = 1000$ and $\alpha = 0.15$. A sharp peak at the interface is the main characteristic of the distribution. The enstrophy increases in time throughout both layers. The enstrophy increase is caused by the action of viscous forces in the liquid layer

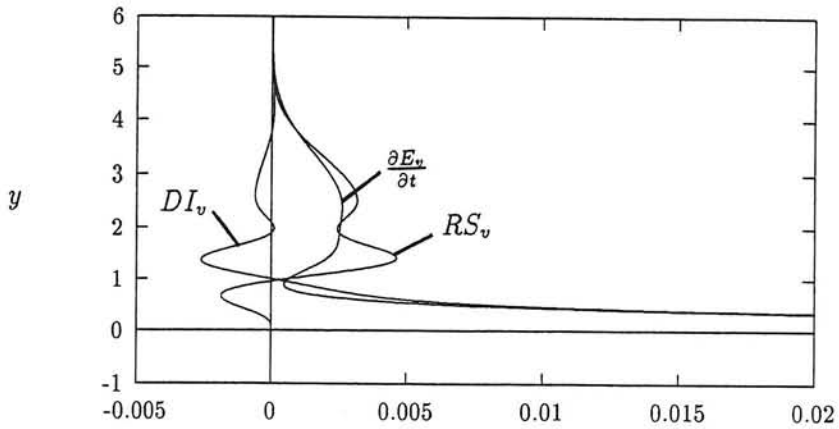


FIGURE 5.11: Enstrophy balance ($y_i = 10, IM = IN = 100, NOP = 2000, m = 1.07 \times 10^4, n = 0.82, r = 1400, Re = 1000, y_w = -1, \alpha = 0.15$)

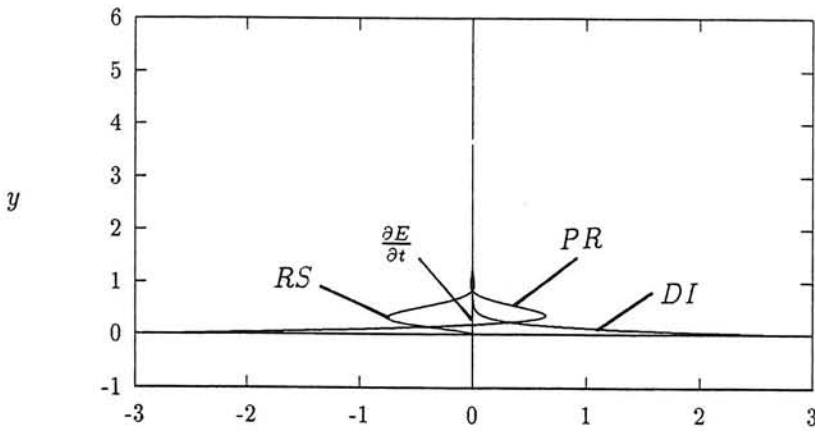


FIGURE 5.12: Mechanical energy balance ($y_i = 10, IM = IN = 100, NOP = 2000, m = 1.07 \times 10^4, n = 0.82, r = 1400, Re = 1000, y_w = -1, \alpha = 0.25$)

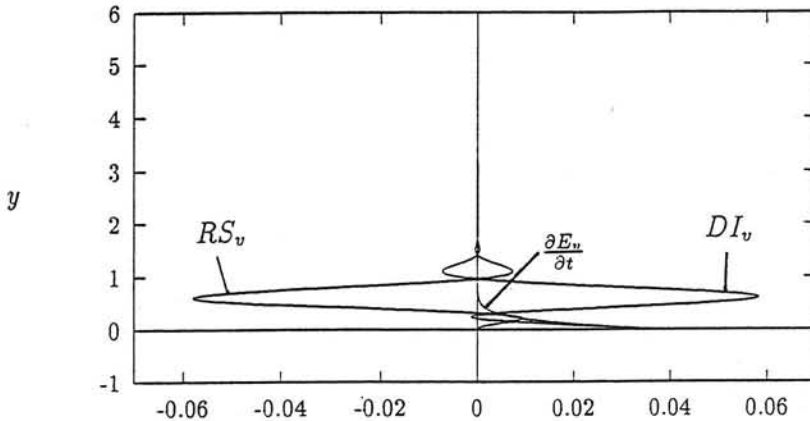


FIGURE 5.13: Entrophy balance ($y_i = 10, IM = IN = 100, NOP = 2000, m = 1.07 \times 10^4, n = 0.82, r = 1400, Re = 1000, y_w = -1, \alpha = 0.25$)

and in the lower region of the gas layer. In the far field, the Reynolds stress causes the increase in entrophy with time. Again, the figure for the upper layer is identical to that found for the one-layer case in the previous chapter.

The mechanical energy distribution for the interfacial mode ($Re = 1000, \alpha = 0.25$) is given in figure 5.12. The kinetic energy increases in time in both layers and is driven by the action of viscosity in the lower layer as well as in the upper layer. The Reynolds stress and the pressure term stabilize the flow.

Finally, the origin of the growth in entrophy with time for the interfacial mode is given in figure 5.13. In the lower layer, the viscous forces are the driving force. In the first part of the upper layer, the viscous forces destabilize the flow, further away from the wall, the Reynolds stress, then again the viscous forces.

5.1.4 Parameters survey

In this subsection, the influence of the density ratio, the depth and the viscosity ratio will be studied. The following values will be used as reference. The virtual interface is set $y_i = 10$, 61 Chebyshev polynomials are used in each fluid layer.

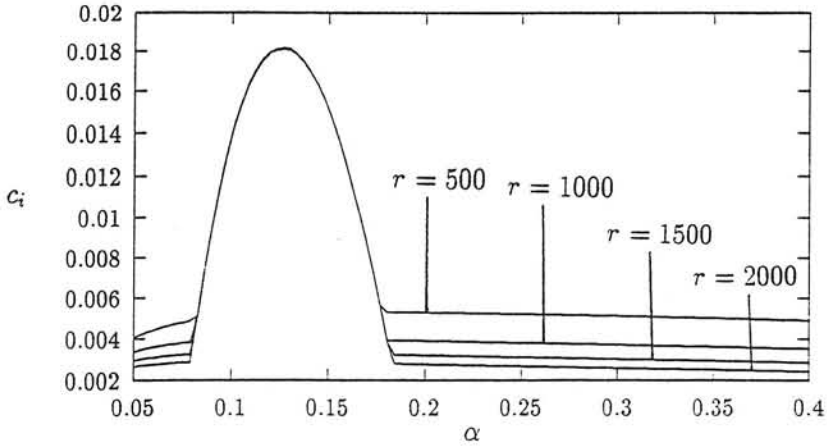


FIGURE 5.14: Stability curves for different density ratios ($y_i = 10, IM = IN = 60, m = 1000, n = 1, Re = 1000, y_w = -1$)

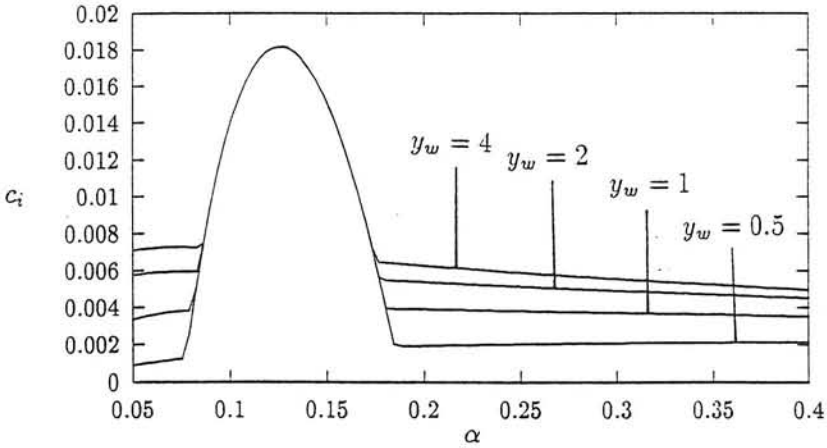


FIGURE 5.15: Stability curves for different depths ($y_i = 10, IM = IN = 60, m = 1000, n = 1, r = 1000, Re = 1000$)

the flow is assumed Newtonian ($n = 1$) and the Reynolds number is set equal to 1000. Furthermore, the density ratio is set at $r = 1000$, the solid wall in the lower fluid layer is at $y_w = -1$ and the viscosity ratio is $m = 1000$.

Figure 5.14 shows the influence of different density ratios. Density ratios of 500, 1000, 1500 and 2000 are plotted. A system of water/air has a ratio of about 1000 and for an anti-icing fluid, the ratio is about 1400. The influence of the density on the lower fluid layer is hardly visible on the Blasius instability. However, the interfacial instability is reduced by increasing the density ratio, as is expected, the lower fluid becoming more solid.

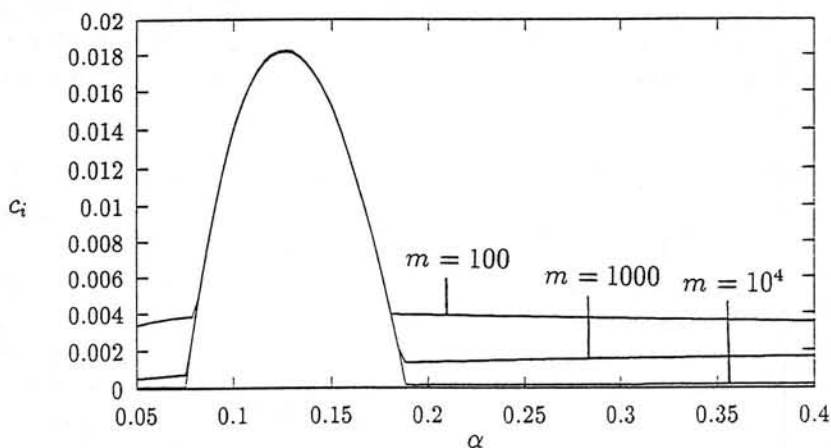


FIGURE 5.16: Stability curves for different viscosity ratios ($y_i = 10, IM = IN = 60, n = 1, r = 1000, Re = 1000, y_w = -1$)

The stability for depths of 0.5, 1, 2 and 4 are given in figure 5.15. These depths correspond to liquid layer of about 1mm to 6mm. The influence of the depth of the fluid layer on the Blasius instability is again negligible. However, by decreasing the depth, the interfacial mode will become more stable. Finally, for viscosity ratios of 100, 1000 and 10^4 . the stability curves are plotted in figure 5.16. As before, the Blasius instability remains unaffected by changing the viscosity ratio. The flow becomes more stable by increasing the viscosity ratio, since the lower fluid layer will act more and more like a solid wall.

5.2 Validation energy considerations

The energy (and enstrophy) distribution integrated in y -direction can be calculated in several different ways. One way is to integrate the distribution, averaged over one wave length, using Simpson's rule. This method can be applied to all terms of the energy distribution. As will become clear later, to obtain a good accuracy of the numerical solution about 2000 points have to be used for the quadrature in each fluid layer. This resolution is needed to represent all features accurately.

The pressure term can be converted using Stokes' theorem, from a surface integral to a contour integral. The contribution of the boundaries at $x = 0$ and $x = \lambda$ cancel. At infinity and at the solid wall, the contribution equals zero. The only contribution can therefore be from the difference between the two fluids on each side of the interface. In a one-layer flow, the contribution from the pressure term equals zero. In the numerical calculations, the pressure term has to be cut-off at the virtual interface instead of at infinity.

Using partial integration, the dissipation term can be rewritten in a term for the inner region of both fluids and a line integral along the boundaries. In case of a Newtonian fluid, the term for the inner region is always less than zero as can be shown easily. This is not the case for a non-Newtonian power-law fluid. The contribution of the boundaries at $x = 0$ and $x = \lambda$ cancel. The contribution at infinity and the solid wall are equal to zero. The only contribution of the boundaries is therefore from both sides of the interface. In case of one-layer Blasius flow, the dissipation term is always less than zero.

The change in kinetic energy can be written as

$$\frac{dE}{dt} = c_i \pi e^{2\alpha c_i t} \left(\alpha^2 |\phi(y)|^2 + \left| \frac{d\phi(y)}{dy} \right|^2 \right) \quad (5.1)$$

Substitution of the Chebyshev polynomials and evaluation of the resulting equations leads to a closed-form expression for the change in kinetic energy without the use of the NOP points in the upper and lower layer. Such an expression can only be obtained for the change in kinetic energy. The following two integrals are needed for the evaluation.

$$\int_{-1}^1 T_m(x) T_n(x) dx = \begin{cases} 0, & \text{for } m - n \text{ odd} \\ \frac{2(m^2+n^2-1)}{(m+n+1)(m+n-1)(m+1-n)(n+1-m)}, & \text{for } m - n \text{ even} \end{cases} \quad (5.2)$$

$$\int_{-1}^1 \frac{dT_m(x)}{dx} \frac{\partial T_n(x)}{\partial x} dx = \begin{cases} 0, & \text{for } m - n \text{ odd} \\ 2mn \sum_{k=\frac{m-n}{2}+1}^{\frac{m+n}{2}} \frac{1}{2k-1}, & \text{for } m - n \text{ even} \end{cases} \quad (5.3)$$

The energy distribution has been computed using the different methods outlined above and the results have been verified. It was shown that corresponding results could only be obtained by using a high (over 1000) quadrature points in each layer.

5.3 Comparison with literature

Yih [41] gives an analytical formula (approximation) for the growth rate of a two-layer system consisting of a de-icing fluid and an air stream. He considers a flat plate covered with a thin layer of liquid and assumes that the viscosity ratio of liquid to air is very high (over half a million). The primary flow consists of a linear velocity profile in both the thin liquid layer and the boundary-layer of the air stream, which is an approximation of the Blasius boundary-layer. On top of the boundary-layer, the flow field is assumed to be uniform. The main results of his study are given in formula (77) and (78) of his article denoting for a given set of parameters the phase velocity and the growth rate, respectively.

Yih applies the formulas derived to a special case. In the notation of this report, Yih's case is characterized by $L^* = 3.08 \times 10^{-4}m$, $y_w = -3.567$, $m = 598802$, $n = 1$, $r = 972$, $Re = 1167$ and $S = 0.1012$ (corresponding to $T = 31.3 \times 10^3 N/m$). These values correspond with Hoechst 1704 de-icing fluid [38]. Yih found that the flow is unstable for wave numbers between 0.0041 and 0.14. Tsao [38] found using the triple-deck theory that the flow is unstable for wave numbers between 0.0025 and 0.37. The numerical computations show that the flow is unstable for wave numbers between 0.0032 and 0.41. The numerical calculations are probably the most accurate results using the least assumptions. They are in fairly good agreement with the triple-deck theory. On the contrary, Yih's results are only of the same order of magnitude. Finally, Yih suggests that the instability arises from the viscosity difference between air and the de-icing fluid, just as the interfacial mode is in this report.

Chapter 6

Conclusions

In this report, the influence of a thin layer of non-Newtonian power-law liquid on the linear temporal stability of a Blasius solution of the flow in a boundary-layer has been investigated.

Blasius' solution without liquid layer is stable for Reynolds numbers, based on the kinematic viscosity of the air, the undisturbed free-stream velocity and the Blasius length scale, below about 300. Above this Reynolds number, a small region of instability appears around a wave number (non-dimensionalized with the Blasius length scale) of about 0.18. By increasing the Reynolds number further, the range of wave numbers for which instability occurs, will increase and shift towards lower wave numbers (longer waves). The linearly unstable wave lengths are about 6 times the Blasius length scale. This mode of instability is referred to as the Blasius mode.

The wave speed of the most unstable wave numbers ranges between 25% and 45% of the undisturbed free stream velocity. The wave speed decreases by increasing the Reynolds number. The x -component (tangential to the wall) of the velocity perturbation shows two distinct maximums in the boundary layer. The larger one of these two is located near the wall and the other one in the neighbourhood of the edge of the boundary layer. This behaviour is present for both stable and unstable modes. On the contrary, the y -component of the velocity perturbation shows only one maximum somewhere midway in the Blasius boundary-layer. There is a phase difference of around $\pi/2$ between the velocity perturbation in x - and the one in y -direction.

The instability in the boundary-layer is driven by the so-called Reynolds stress term, the interaction between the primary flow and the perturbation velocities. The influence of viscosity (dissipation term) is stabilizing. By looking at the energy distribution throughout the layer, the pressure term, due to the interaction of the perturbation in the pressure and the perturbation velocities, destabilizes the flow near the solid wall. Further away from the wall, the pressure terms stabilize the flow. The overall net effect of the pressure term adds up to zero.

The introduction of a thin layer of liquid between the solid wall and the Blasius boundary-layer does not affect the Blasius mode instability very much. The same features as in the one-layer case are also present in the two-layer case. However, the liquid layer introduces another mode of instability, the so-called interfacial mode of instability. This mode is characterized by very low wave speeds (around 10^{-5} with respect to the free-stream velocity) and growth rates of the same order of magnitude. Furthermore, there is a very large range of unstable wave numbers for this mode. However, the results should be interpreted cautiously, as the amplitude of the air/liquid interface displacement is large compared to the assumed order of the interface displacement.

The velocity and the pressure perturbations in the thin liquid layer are several orders of magnitude smaller than the corresponding perturbation quantities in the Blasius boundary-layer. The interfacial instability is caused by the difference in viscosity between the two fluid layers, as also suggested by Yih [41]. For this mode, the Reynolds stress term and the pressure term stabilize the flow.

A parameter survey has been performed for the density ratio, the depth and the viscosity ratio. The effects of these parameters on the Blasius instability is negligibly small. However, the interfacial instability is reduced by increasing the density ratio, i.e., the thin liquid layer will behave more like a solid wall when increasing the density ratio. By decreasing the thickness of the thin liquid layer, the instability of the interfacial mode decreases. And finally, by increasing the viscosity of the thin liquid layer, the instability of the interfacial mode decreases.

References

- [1] Fokker wingtips - how best to fly and maintain your fokker aircraft, April 1992.
- [2] M. Abramowitz and I.A. Segun. *Handbook of Mathematical Functions*. Dover Publications, Inc., New York, 1964.
- [3] O.J. Boelens. An overview of de-icing/anti-icing practice. Technical report, Delft University of Technology, to be published, Delft, 1995.
- [4] T. Brook Benjamin. Shearing flow over a wavy boundary. *Journal of Fluid Mechanics*, 6:161-205, 1959.
- [5] T. Brooke Benjamin. Wave formation in laminar flow down an inclined plane. *Journal of Fluid Mechanics*, 2:554-574, 1957.
- [6] G.J. de Bruin. Stability of a layer of liquid flowing down an inclined plane. *Journal of Engineering Mathematics*, 8 - 3:259-271, 1974.
- [7] C. Canuto, M.Y. Hussaini, A. Quarteroni, and T.A. Zang. *Spectral methods in fluid dynamics*. Springer Series in Computational Physics. Springer-Verlag, Berlin, 1988.
- [8] M. Carbonaro. Aerodynamic effects of de-/anti-icing fluids and description of a facility and test technique for their assessment. In *AGARD conference proceedings 496 on effects of adverse weather on aerodynamics*, Toulouse, 1991.
- [9] P.G. Drazin and W.H. Reid. *Hydrodynamic stability*. Cambridge Monographs on Mechanics and Applied Mathematics. Cambridge University Press, Cambridge, 1981.

- [10] S. Feldman. On the hydrodynamic stability of two viscous incompressible fluids in parallel uniform shearing motion. *Journal of Fluid Mechanics*, 2:343-370, 1957.
- [11] J.M. Floryan, S.H. Davis, and R.E. Kelly. Instabilities of a liquid film flowing down a slightly inclined plane. *Physics of Fluids*, 30:983-989, 1987.
- [12] J. Harris. *Rheology and non-Newtonian flow*. Longman, London, 1978.
- [13] W. Heisenberg. Uber stabilitat und turbulenz von flussigkeitsstromen. *Ann. Phys. Lpz.*, 74:577, 1924.
- [14] E.J. Hinch. A note on the mechanism of the instability at the interface between two shearing fluids. *Journal of Fluid Mechanics*, 144:463-465, 1984.
- [15] A.P. Hooper. Long-wave instability at the interface between two viscous fluids: Thin layer effects. *Physics of Fluids*, 28:1613-1618, 1985.
- [16] A.P. Hooper and W.G.C. Boyd. Shear-flow instability at the interface between two viscous fluids. *Journal of Fluid Mechanics*, 128:507-528, 1983.
- [17] A.P. Hooper and W.G.C. Boyd. Shear-flow instability due to a wall and a viscosity discontinuity at the interface. *Journal of Fluid Mechanics*, 179:201-225, 1987.
- [18] T.W. Kao. Role of viscosity stratification in the stability of two-layer flow down an incline. *Journal of Fluid Mechanics*, 33:561-572, 1968.
- [19] H. Lamb. *Hydrodynamics*. Cambridge University Press, Cambridge, 1932.
- [20] L.D. Landau and E.M. Lifshitz. *Fluid Mechanics*. Course of Theoretical Physics, volume 6. Pergamon Press Ltd., Oxford, Second Edition, 1987.
- [21] S.P. Lin. Film waves. In R.E. Meyer, editor, *Waves on fluid interfaces*, 1983.
- [22] R. Miesen, G. Beijnon, P.E.M. Duijvestijn, R.V.A. Oliemans, and T. Verheggen. Interfacial waves in core-annular flow. *Journal of Fluid Mechanics*, 238:97-117, 1992.
- [23] R. Miesen and B.J. Boersma. Hydrodynamic stability of a sheared liquid film. *Journal of Fluid Mechanics*, 301:175-202, 1995.

- [24] J.W. Miles. The hydrodynamic stability of a thin film of liquid in uniform shearing motion. *Journal of Fluid Mechanics*, 8:593-610, 1960.
- [25] P.J.J. Moeleker. Hydrodynamic stability of a liquid layer subjected to shear. Technical report, Delft University of Technology, Delft, January 1996. M.Sc. thesis.
- [26] C.B. Moler and G.W. Stewart. An algorithm for generalized matrix eigenvalue problems. *SIAM J. Numer. Anal.*, 10 - 2:241-256, 1973.
- [27] W.Mc.F. Orr. *Proc. Roy. Irish Acad.*, 27, 1906.
- [28] S.A. Orszag. Accurate solution of the orr-sommerfeld stability equation. *Journal of Fluid Mechanics*, 50:689-703, 1971.
- [29] S. Ozgen. Stability of parallel non-newtonian flows. Technical report, Von Kármán Institute for Fluid Dynamics, Rhode Saint Genese, June 1995.
- [30] M.C. Potter. Stability of plane couette-poiseuille flow. *Journal of Fluid Mechanics*, 24 - 3:609-619, 1966.
- [31] Y. Renardy. Instability at the interface between two shearing fluids in a channel. *Physics of Fluids*, 28(12):3341-3443, 1985.
- [32] O. Rumberg. Two-layer flow instability. Technical report. Von Kármán Institute for Fluid Dynamics, Rhode Saint Genese, June 1995.
- [33] H. Schlichting. *Boundary-layer Theory*. McGraw-Hill series in Mechanical Engineering. McGraw-Hill Book Company, New York, USA, 1968.
- [34] M.K. Smith. The mechanism for the long-wave instability in thin liquid films. *Journal of Fluid Mechanics*, 217:469-485, 1990.
- [35] M.K. Smith and S.H. Davis. The instability of sheared liquid layers. *Journal of Fluid Mechanics*, 121:187-206, 1982.
- [36] A. Sommerfeld. *Atti del IV Congresso Internazionale dei Matematici*, 3:116, 1909.
- [37] H.B. Squire. *Proc. Roy. Soc.*, 142:621, 1933.
- [38] J.-C. Tsao, A.P. Rothmayer, and A.I. Ruban. Stability of air flow past thin liquid films on airfoils. *AIAA 96-2155*, 1996.

- [39] J.H. Wilkinson. *The algebraic eigenvalue problem*. Monographs on numerical analysis. Oxford University Press, Oxford, 1965.
- [40] C.-S. Yih. Instability due to viscosity stratification. *Journal of Fluid Mechanics*, 27:337-352, 1967.
- [41] C.-S. Yih. Wave formation on a liquid layer for de-icing airplane wings. *Journal of Fluid Mechanics*, 212:41-53, 1990.

Series 01: Aerodynamics

01. F. Motallebi, 'Prediction of Mean Flow Data for Adiabatic 2-D Compressible Turbulent Boundary Layers'
1997 / VI + 90 pages / ISBN 90-407-1564-5
02. P.E. Skåre, 'Flow Measurements for an Afterbody in a Vertical Wind Tunnel'
1997 / XIV + 98 pages / ISBN 90-407-1565-3
03. B.W. van Oudheusden, 'Investigation of Large-Amplitude 1-DOF Rotational Galloping'
1998 / IV + 100 pages / ISBN 90-407-1566-1
04. E.M. Houtman / W.J. Bannink / B.H. Timmerman, 'Experimental and Computational Study of a Blunt Cylinder-Flare Model in High Supersonic Flow'
1998 / VIII + 40 pages / ISBN 90-407-1567-X
05. G.J.D. Zondervan, 'A Review of Propeller Modelling Techniques Based on Euler Methods'
1998 / IV + 84 pages / ISBN 90-407-1568-8
06. M.J. Tummers / D.M. Passchier, 'Spectral Analysis of Individual Realization LDA Data'
1998 / VIII + 36 pages / ISBN 90-407-1569-6
07. P.J.J. Moeleker, 'Linear Temporal Stability Analysis'
1998 / VI + 74 pages / ISBN 90-407-1570-X
08. B.W. van Oudheusden, 'Galloping Behaviour of an Aeroelastic Oscillator with Two Degrees of Freedom'
1998 / IV + 128 pages / ISBN 90-407-1571-8
09. R. Mayer, 'Orientation on Quantitative IR-thermography in Wall-shear Stress Measurements'
1998 / XII + 108 pages / ISBN 90-407-1572-6
10. K.J.A. Westin / R.A.W.M. Henkes, 'Prediction of Bypass Transition with Differential Reynolds Stress Models'
1998 / VI + 78 pages / ISBN 90-407-1573-4
11. J.L.M. Nijholt, 'Design of a Michelson Interferometer for Quantitative Refraction Index Profile Measurements'
1998 / 60 pages / ISBN 90-407-1574-2
12. R.A.W.M. Henkes / J.L. van Ingen, 'Overview of Stability and Transition in External Aerodynamics'
1998 / IV + 48 pages / ISBN 90-407-1575-0
13. R.A.W.M. Henkes, 'Overview of Turbulence Models for External Aerodynamics'
1998 / IV + 40 pages / ISBN 90-407-1576-9

Series 02: Flight Mechanics

01. E. Obert, 'A Method for the Determination of the Effect of Propeller Slipstream on a Static Longitudinal Stability and Control of Multi-engined Aircraft'
1997 / IV + 276 pages / ISBN 90-407-1577-7
02. C. Bill / F. van Dalen / A. Rothwell, 'Aircraft Design and Analysis System (ADAS)'
1997 / X + 222 pages / ISBN 90-407-1578-5
03. E. Torenbeek, 'Optimum Cruise Performance of Subsonic Transport Aircraft'
1998 / X + 66 pages / ISBN 90-407-1579-3

Series 03: Control and Simulation

01. J.C. Gibson, 'The Definition, Understanding and Design of Aircraft Handling Qualities'
1997 / X + 162 pages / ISBN 90-407-1580-7
02. E.A. Lomonova, 'A System Look at Electromechanical Actuation for Primary Flight Control'
1997 / XIV + 110 pages / ISBN 90-407-1581-5
03. C.A.A.M. van der Linden, 'DASMAT-Delft University Aircraft Simulation Model and Analysis Tool. A Matlab/Simulink Environment for Flight Dynamics and Control Analysis'
1998 / XII + 220 pages / ISBN 90-407-1582-3

Series 05: Aerospace Structures and Computational Mechanics

01. A.J. van Eekelen, 'Review and Selection of Methods for Structural Reliability Analysis'
1997 / XIV + 50 pages / ISBN 90-407-1583-1
02. M.E. Heerschap, 'User's Manual for the Computer Program Cufus. Quick Design Procedure for a CUt-out in a FUSelage version 1.0'
1997 / VIII + 144 pages / ISBN 90-407-1584-X
03. C. Wohlever, 'A Preliminary Evaluation of the B2000 Nonlinear Shell Element Q8N.SM'
1998 / IV + 44 pages / ISBN 90-407-1585-8
04. L. Gunawan, 'Imperfections Measurements of a Perfect Shell with Specially Designed Equipment (UNIVIMP)'
1998 / VIII + 52 pages / ISBN 90-407-1586-6

Series 07: Aerospace Materials

01. A. Vašek / J. Schijve, 'Residual Strength of Cracked 7075 T6 Al-alloy Sheets under High Loading Rates'
1997 / VI + 70 pages / ISBN 90-407-1587-4
02. I. Kunes, 'FEM Modelling of Elastoplastic Stress and Strain Field in Centre-cracked Plate'
1997 / IV + 32 pages / ISBN 90-407-1588-2
03. K. Verolme, 'The Initial Buckling Behavior of Flat and Curved Fiber Metal Laminate Panels'
1998 / VIII + 60 pages / ISBN 90-407-1589-0
04. P.W.C. Provó Kluit, 'A New Method of Impregnating PEI Sheets for the *In-Situ* Foaming of Sandwiches'
1998 / IV + 28 pages / ISBN 90-407-1590-4
05. A. Vlot / T. Soerjanto / I. Yeri / J.A. Schelling, 'Residual Thermal Stresses around Bonded Fibre Metal Laminate Repair Patches on an Aircraft Fuselage'
1998 / IV + 24 pages / ISBN 90-407-1591-2
06. A. Vlot, 'High Strain Rate Tests on Fibre Metal Laminates'
1998 / IV + 44 pages / ISBN 90-407-1592-0
07. S. Fawaz, 'Application of the Virtual Crack Closure Technique to Calculate Stress Intensity Factors for Through Cracks with an Oblique Elliptical Crack Front'
1998 / VIII + 56 pages / ISBN 90-407-1593-9
08. J. Schijve, 'Fatigue Specimens for Sheet and Plate Material'
1998 / VI + 18 pages / ISBN 90-407-1594-7

Series 08: Astrodynamics and Satellite Systems

01. E. Mooij, 'The Motion of a Vehicle in a Planetary Atmosphere'
1997 / XVI + 156 pages / ISBN 90-407-1595-5
02. G.A. Bartels, 'GPS-Antenna Phase Center Measurements Performed in an Anechoic Chamber'
1997 / X + 70 pages / ISBN 90-407-1596-3
03. E. Mooij, 'Linear Quadratic Regulator Design for an Unpowered, Winged Re-entry Vehicle'
1998 / X + 154 pages / ISBN 90-407-1597-1

The first part of the report deals with the general situation of the country. It is noted that the population is increasing rapidly, and that the government is making every effort to improve the living conditions of the people. The report also mentions the progress of the various departments of the government, and the success of the various public works projects.

The second part of the report deals with the financial situation of the country. It is noted that the government has managed to maintain a balanced budget, and that the public debt is being reduced. The report also mentions the success of the various public works projects, and the progress of the various departments of the government.

The third part of the report deals with the social situation of the country. It is noted that the government is making every effort to improve the living conditions of the people, and that the various public works projects are being completed. The report also mentions the success of the various departments of the government, and the progress of the various public works projects.

The fourth part of the report deals with the political situation of the country. It is noted that the government is making every effort to improve the living conditions of the people, and that the various public works projects are being completed. The report also mentions the success of the various departments of the government, and the progress of the various public works projects.

The fifth part of the report deals with the economic situation of the country. It is noted that the government is making every effort to improve the living conditions of the people, and that the various public works projects are being completed. The report also mentions the success of the various departments of the government, and the progress of the various public works projects.

The sixth part of the report deals with the military situation of the country. It is noted that the government is making every effort to improve the living conditions of the people, and that the various public works projects are being completed. The report also mentions the success of the various departments of the government, and the progress of the various public works projects.

The seventh part of the report deals with the foreign relations of the country. It is noted that the government is making every effort to improve the living conditions of the people, and that the various public works projects are being completed. The report also mentions the success of the various departments of the government, and the progress of the various public works projects.

3021863

An infinite flat plate covered with a thin layer of a power-law fluid sheared by an air stream is considered. The equations and boundary conditions governing the temporal linear stability problem are derived assuming small disturbances superimposed on a steady primary flow. The latter consists of a Blasius boundary-layer flow for the air stream and an exact solution of the Navier-Stokes equations for the thin fluid layer. Sources of change in kinematic energy and enstrophy are identified. A spectral collocation method based on Chebyshev polynomials is implemented and the resulting algebraic problem is solved using a QZ-algorithm. An isolated Blasius boundary-layer flow showed instability above a critical Reynolds number (approx. 300) for a range of wave numbers (Blasius mode). The presence of a thin fluid layer introduced, next to the (hardly changed) Blasius mode, an additional unstable mode (interfacial mode) exhibiting smaller amplification rates and a larger range of instability. The Blasius mode instability is driven mainly by the Reynolds stress and the interfacial mode by the action of viscosity. This research has been carried out within the framework of predicting the dynamic behaviour of a thin layer of liquid (e.g. water or anti-icing fluid) sheared by an air flow.

ISBN 90-407-1570-X



9 799040 715708

